Received: 2 February 2023 | Revised: 17 July 2023 | Accepted: 19 July 2023

DOI: 10.1002/msd2.12081

REVIEW ARTICLE

IJMSD International Journal of Mechanical System Dynamics Open Access WILEY

# Probing electron and lattice dynamics by ultrafast electron microscopy: Principles and applications

Yiling Lian[1] | Jingya Sun[1,2] | Lan Jiang[1,2,3]

[1]Laser Micro/Nano Fabrication Laboratory, School of Mechanical Engineering, Beijing Institute of Technology, Beijing, P.R. China

[2]Yangtze Delta Region Academy of Beijing Institute of Technology, Jiaxing, P.R. China

[3]Chongqing Innovation Center, Beijing Institute of Technology, Chongqing, P.R. China

**Correspondence**

Prof. Lan Jiang, Laser Micro/Nano Fabrication Laboratory, School of Mechanical Engineering, Beijing Institute of Technology, Beijing 100081, P.R. China.
Email: jianglan@bit.edu.cn

## Abstract

Microscale charge and energy transfer is an ultrafast process that can determine the photoelectrochemical performance of devices. However, nonlinear and nonequilibrium properties hinder our understanding of ultrafast processes; thus, the direct imaging strategy has become an effective means to uncover ultrafast charge and energy transfer processes. Due to diffraction limits of optical imaging, the obtained optical image has insufficient spatial resolution. Therefore, electron beam imaging combined with a pulse laser showing high spatial–temporal resolution has become a popular area of research, and numerous breakthroughs have been achieved in recent years. In this review, we cover three typical ultrafast electron beam imaging techniques, namely, time-resolved photoemission electron microscopy, scanning ultrafast electron microscopy, and ultrafast transmission electron microscopy, in addition to the principles and characteristics of these three techniques. Some outstanding results related to photon–electron interactions, charge carrier transport and relaxation, electron–lattice coupling, and lattice oscillation are also reviewed. In summary, ultrafast electron beam imaging with high spatial–temporal resolution and multidimensional imaging abilities can promote the fundamental understanding of physics, chemistry, and optics, as well as guide the development of advanced semiconductors and electronics.

**KEYWORDS**

ultrafast electron imaging, charge transfer, time-resolved photoemission electron microscopy, scanning ultrafast electron microscopy, ultrafast transmission electron microscopy

## 1 | INTRODUCTION

Ultrafast science is an important aspect of modern scientific research that involves exploring the dynamic behaviors of microscopic particles[1–5] and developing strategies[6–12] to elucidate these behaviors through ultrahigh spatial and temporal resolution. This technique allows researchers to understand, apply, and control the related physics,[13–15] chemistry,[16,17] and other macroscopic phenomena[18–20] of these particles. The emergence of ultrashort pulse laser technology[21–26] offers an excellent strategy for studying this problem. Ultrashort lasers use extremely short periods of light exposure,[27–29] providing an unprecedented shutter speed for photographing the motion of microscopic particles,[30–34] where, the shorter the pulse width of the laser pulse, the faster the shutter speed. Thus, generating shorter laser pulses has become an important aspect of

Yiling Lian and Jingya Sun contributed equally to this study.

ultrafast science.[35,36] The progress in femtosecond lasers has led to ultrafast time-resolved measurements,[37–39] which have directly contributed to the rapid development of ultrafast science fields represented by femtosecond chemistry/physics.[40–42] In the 1990s, Zewail[43] used a femtosecond pump–probe experiment to realize ultrafast process detection on the femtosecond time scale, successfully observing the motion process of atoms during the chemical reaction process,[44] for which Zewail[45] won the Nobel Prize in Chemistry in 1999. In the 2000s, reflection pump–probe technology was used to study the carrier dynamics of materials, indicating a strong difference between electrons and hole relaxation behavior after initial intraband relaxation in CdSe nanocrystals.[46] The study revealed two distinct time scales associated with the relaxation of nonequilibrium photogenerated carriers in epitaxial graphene,[47] demonstrating a longer carrier lifetime in the core-shell quantum dot (QD) than in the QD.[48] In 2010, Shigekawa and colleagues included a scanning tunneling microscope in the pump–probe experiment,[49] which could be used to study the dynamic process of carrier migration in semiconductors, realizing ultrafast atomic-level observations in real space. In recent years, the laser pulse width has been compressed, due to the development of pulse compression technology, and the time resolution of the pump–probe technique has been improved to less than 20 fs.[39] Although in situ electrothermal magnetic fields can allow the pump–probe technique to capture more novel phenomena,[50,51] the spatial resolution will likely become non-negligible during these processes.

Both electron relaxation/jumping and lattice vibrations accompanied by spatial variations can be transmitted at ultrafast speeds[52–54] (picosecond–femtosecond) within very small scales[55,56] (micron–nanometer). When photons are absorbed by electrons, forming transferable charge carriers, the charge carrier will diffuse and relax[57–60] through both equilibrium and nonequilibrium paths, such as ballistic transport,[61,62] inelastic scattering,[63,64] and electron and phonon interactions.[18,33,65] The investigation of ultrafast carrier transfer on the nanoscale and profound changes in various physical parameters presents a formidable challenge for theoretical models. To analyze these intricate processes, direct imaging[31,66,67] using cameras has been proposed to determine distinct carrier transfer pathways.[68] However, direct imaging requires more than 10 000 exposures to avoid inherent noise of the experimental systems and environmental factors. This provides a simple but less efficient solution. Consequently, the development of a nondestructive ultrafast imaging technique that can detect weak signals has become imperative. Transient absorption microscopy[69] utilizes a stationary pump beam with a scanning probe beam that systematically interrogates the pumped region. Despite the diffraction limit of the laser,[70–73] this method can be used to study the charge carrier dynamics with precise spatiotemporal resolution. However, the laser pulses have substantial penetration depths, making them less suitable for surface-specific probing. The reconstruction strategy, inspired by the extraordinarily short wavelength of electrons, has generated interest in utilizing ultrafast electron beams for imaging, resulting in electron imaging with nanometer or subnanometer resolutions.[40,74,75] The combination of ultrafast laser and electron beam imaging can seamlessly integrate high temporal and spatial resolutions.[76–85] For example, to achieve the high-resolution imaging of surface carrier dynamics, a probe laser pulse can excite an electron gun and generate a pulsed electron beam that subsequently interacts with the sample for imaging. To reveal carrier transfer at interfaces due to an intricate band structure, the probe laser pulse will excite the pumped sample and induce electron spillover from the surface for imaging. Meanwhile, to explore the dynamics of lattice evolution, the probe electron pulse will hit the sample and the traversed electrons can be collected for imaging.

Ultrafast electron beam imaging holds significant potential for microscale applications. Three types of commonly used ultrafast electron imaging methods exist: time-resolved photoemission electron microscopy (TR-PEEM), scanning ultrafast electron microscopy (SUEM), and ultrafast transmission electron microscopy (UTEM). In this article, we present the technical principles and list the scope of applications according to the equipment characteristics, focusing on the electron dynamics of femtosecond laser excitation for different material systems. Specifically, we explore the following areas: (1) surface plasmon polaritons (SPP) and photocatalysis using TR-PEEM; (2) anomalous carrier transport in silicon, defect-affected carrier dynamics in InGaN, and carrier relaxation/diffusion in single crystals, as revealed by SUEM; and (3) the lattice vibrations in transition-metal dihalides (TMDs) and microscale phase transition in metals, utilizing UTEM.

## 2 | PRINCIPLES

All three ultrafast electron imaging methods utilize steady-state imaging and femtosecond laser pump–probe techniques. The process begins with the pump beam, which is directed at the sample and used to excite the sample, causing a density/temperature/energy-level change of electrons. This results in subsequent charge and energy transfer processes. After a certain delay, the probe beam can be used to excite the sample or electron gun, producing an ultrafast electron beam that can be detected by the detector. This can be used to achieve high spatial–temporal resolutions.

### 2.1 | Principles of TR-PEEM

PEEM utilizes an electron microscope to image the distribution of photoelectron emissions on surface samples based on the photoelectric effect.[86] Two main imaging modes are used in PEEM. (1) The first is geometric mode, where different morphologies of the sample surface will cause a change in photoelectron emission direction, resulting in different spatial distributions of detected electron emissions. (2) The second mode involves the work function/electron density of states. In this mode, for a photon with a specific energy, differences in the power function or electron density of states of materials will also cause differences in the amount of electron emissions. For TR-PEEM, an ultrafast laser beam can be divided into two subbeams. One can be used for sample excitation, while the other can be used to excite surface photoelectron emissions. When the probe beam is coincident with the pump beam at the sample surface, the probe beam-induced photoelectron will change as the

excitation gradually transforms into the ground state; thus, the number and energy of photoemission of the electrons can be detected at different probe delays.[87] Therefore, PEEM has been successfully combined with femtosecond lasers, known as TR-PEEM, as shown in Figure 1.

## 2.2 | Principles of SUEM

Scanning electron microscopy (SEM) involves controlling an electron beam to scan a specific area point by point, collecting secondary electrons or backscattered electron signals from the electron beam excited area for imaging.[88,89] The secondary electrons primarily reveal morphological features and can image surface micro/nanostructures, while backscattering mainly shows the composition, measures the grain orientations, and analyzes the stress and strain. Two approaches can be used for generating an electron beam generation in SEM.[89] The first involves adding a strong electric field to the filament surface, so that the electrons inside the filament overflow, forming an electron beam. The other involves increasing the temperature so that the electrons inside the filament gain enough kinetic energy to break away from the filament surface. A femtosecond laser can be introduced into an SEM,[40,90] which can be divided into two beams. One beam can act as the pump beam to excite the sample, causing an ultrafast change in the sample. The other can be used to excite the tip of the filament for an ultrashort electron beam[81] (Figure 2). Compared to the unexcited sample, conduction band electrons will have a higher probability of emitting electrons above the vacuum level when scattered by the primary photoelectron pulse. Moreover, their electron emission probability will decrease with electron relaxation. This can cause the image contrast to vary with a probe delay. SUEM offers spatial resolution comparable to SEM, while also providing femtosecond temporal resolution, making it suitable for ultrafast surface science exploration.[91]

## 2.3 | Principles of UTEM

In TEM, the generation of an ultrafast electron beam is similar to SEM. However, the difference lies in how TEM collects transmitted electrons to construct images. TEM allows for high-resolution imaging in real space (imaging), inverted space (diffraction), and energy space (spectroscopy),[92] enabling the observation of structural phase transitions, electron energy loss, and lattice oscillations. Moreover, TEM imaging does not require point-by-point scanning with an electron beam. Instead, it only requires that the detector accumulate a strong enough electron signal to complete the imaging process. When femtosecond lasers are introduced in TEM (Figure 3), two imaging modes can be utilized: strobe and single shot. When imaging in strobe mode, each electron pulse contains a small number of electrons (i.e., about 1–1000 electrons), which can effectively eliminate Coulombic repulsion between the electrons, thus improving the spatial resolution.[94] This mode can be utilized for phenomena that are reversible and repeatable within a certain time scale. By contrast, when imaging in single-shot mode, an electron pulse will contain $10^6$–$10^8$ electrons. Therefore, this imaging mode is primarily used for tracking irreversible processes.[16]

# 3 | SPECIFIC APPLICATIONS OF THE THREE ULTRAFAST ELECTRON IMAGING TECHNIQUES

As previously mentioned, the electron imaging method has its own unique characteristics, with a wide range of applications, as shown in Figure 4. In TR-PEEM, a photon beam serves as the detection tool, and the laser-induced surface spillover electron can be collected for imaging. The spatial distribution of electron energy/density evolution

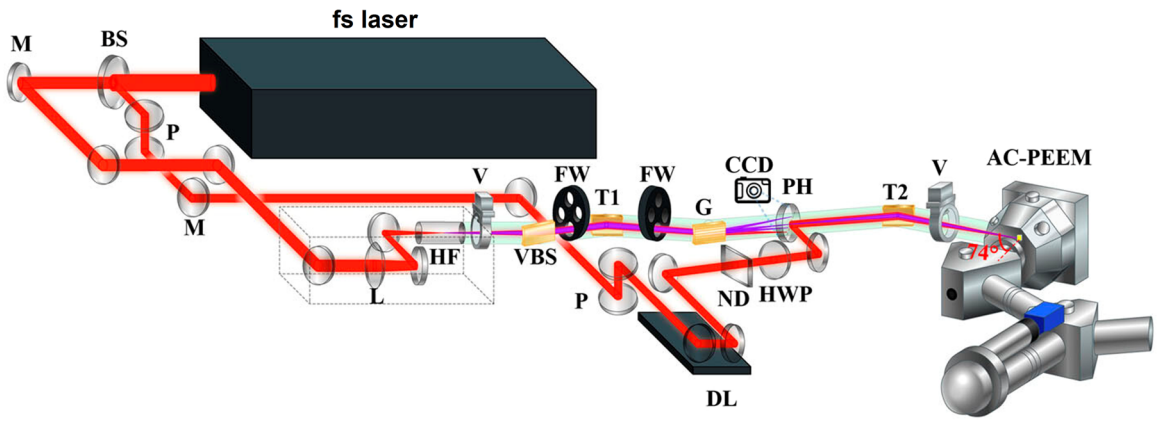


**FIGURE 1** Conceptual diagram showing an ultrafast photoemission electron microscope. The optical path is briefly drawn, with the beam propagating through optical elements such as a fractional mirror (BS), a reflector (mirror), and an attenuator (ND) to finally reach the sample surface. The figure illustrates infrared wavelength light for pumping, and extreme ultraviolet light can be used to excite the surface to produce spillover electrons for detection, while the delay stage (DL) can be adjusted the provide the entire system with a femtosecond to nanosecond time resolution capability. Reproduced under terms of the CC-BY license.[87] Copyright 2021, The Authors, published by AIP. BS, beam splitter; DL, delay line; FW, filter wheel; G, grating; HF, hollow fiber; HWP, half wave plate; L, lens; M, reflective mirror; ND, neutral density filters; P, periscope; PEEM, photoemission electron microscope; PH, pinhole module containing an EUV scintillator; T1, first toroidal mirror; T2, second toroidal mirror 2; V, valve; VBS, vacuum beam splitter.

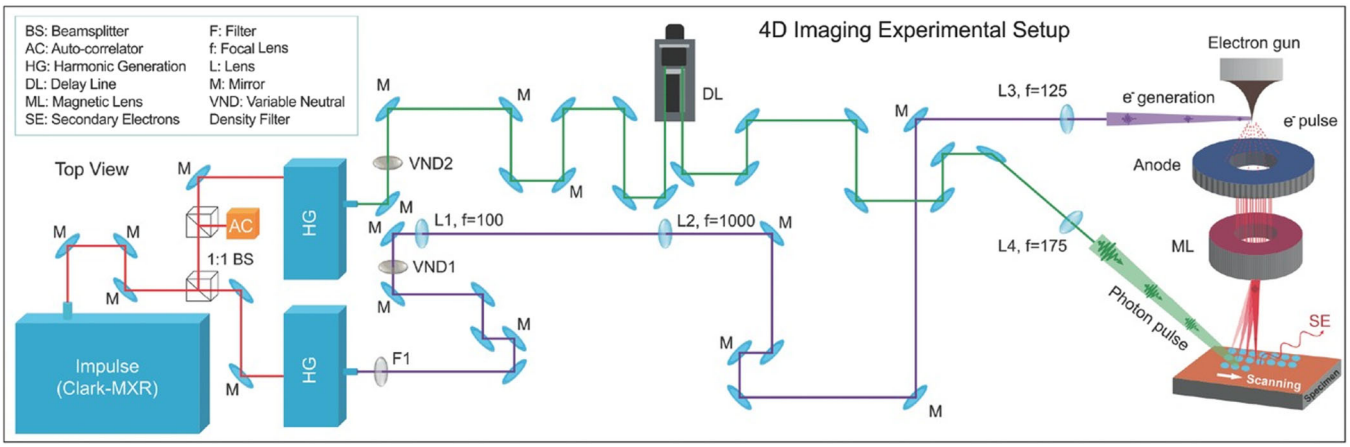


**FIGURE 2** A conceptual diagram of scanning ultrafast electron microscopy, where the sample surface is excited by green light, causing the carrier concentration to change, and the electron gun can be excited by ultraviolet light, generating an electron pulse at the femtosecond level. After this electron pulse acts on the sample surface, secondary electrons will be generated, and the electromagnetic field will be controlled, deflecting the electron pulse, allowing the entire surface to be scanned and used to reconstruct the time-resolved secondary electron image. Reproduced with permission.[81] Copyright 2016, Wiley-VCH.

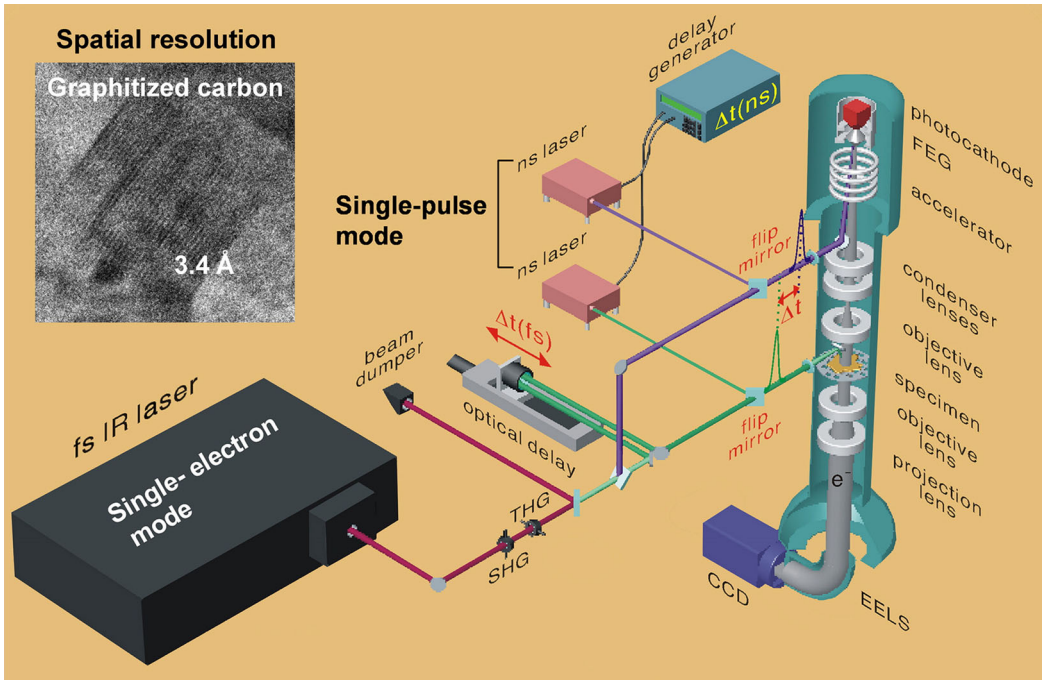


**FIGURE 3** Schematic diagram showing ultrafast electron microscopy using a high-resolution image of graphitized carbon as an example. The principles of excitation and probing of the sample are similar to scanning ultrafast electron microscopy, but ultrafast transmission electron microscopy uses direct imaging with a camera with energy spectrum resolution. In terms of delay adjustment, a nanosecond laser and a signal generator can be added for synergy as a signal acquisition method, achieving delays longer than a nanosecond. Reproduced with permission.[93] Copyright 2009, Elsevier. EELS, electron energy loss spectroscopy; FEG, field emission gun; ns, nanosecond; SHG, second harmonic generation; THG, second harmonic generation.

can be observed by adjusting the delay time. This method can be used to reveal the mechanism of laser interactions with the excited matter/structure. For TR-PEEM, dynamics after photoexcitation can be divided into two types. The first involves the preparation of electromagnetic waves on the surface after pump light excitation. The second involves the dynamic change of the work function of electron escape on the material surface after pump light excitation. This section reviews the dynamics of SPPs and the charge carrier transfer processes according to the changes in the photoemission electron signal. In SUEM, an electron beam can be used as a probing tool, and the collected surface spillover electrons can be utilized for imaging. This method can be used primarily to observe

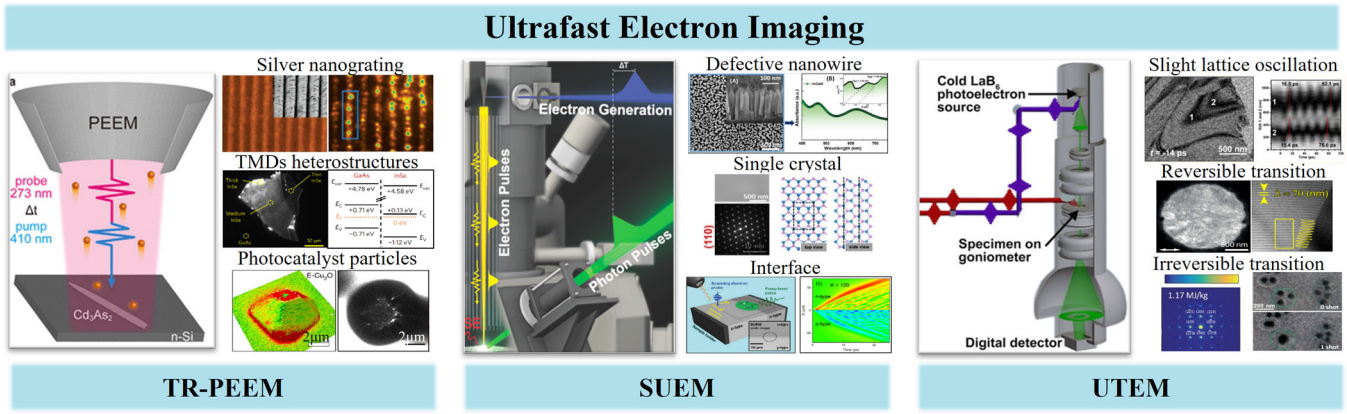


**FIGURE 4** Schematic diagram showing ultrafast electron imaging in terms of applications, including typical applications of TR-PEEM. Reproduced with permission.[4] Copyright 2005, ACS. Reproduced with permission.[95] Copyright 2016, Springer Nature. Reproduced with permission.[96] Copyright 2022, Springer Nature. Reproduced with permission.[97] Copyright 2022, ACS. SUEM, Reproduced with permission.[62] Copyright 2015, AAAS. Reproduced with permission.[98] Copyright 2017, ACS. Reproduced with permission.[99] Copyright 2016, Wiley-VCH. Reproduced with permission.[100] Copyright 2021, APS. Reproduced with permission.[101] Copyright 2019, Elsevier. and UTEM, Reproduced with permission.[102] Copyright 2015, ACS. Reproduced with permission.[103] Copyright 2021, AAAS. Reproduced with permission.[104] Copyright 2018, ACS. Reproduced with permission.[105] Copyright 2019, ACS. Reproduced with permission.[106] Copyright 2018, AAAS. SUEM, scanning ultrafast electron microscopy; TMD, transition-metal dihalide; TR-PEEM, time-resolved photoemission electron microscopy; UTEM, ultrafast transmission electron microscopy.

high-resolution surface carrier dynamics, which play an irreplaceable role in samples with surface micro- and nanostructures. Therefore, the analysis of carrier dynamics under SUEM involves classifying materials into categories such as single crystals, defective/structured surfaces, and heterostructures/interfaces, based on the characteristics of the material being probed. In UTEM, the spatial distribution of transmitted electrons can be imaged using real-, inverse-, and energy-space modes. This may be especially suitable for the high-resolution detection of lattice oscillations and phase transitions. Therefore, this section of the review can be divided into two parts: (a) classification based on the properties of lattice vibrations, encompassing phonon mode studies for small-amplitude vibrations, and reversible phase transitions when the vibration amplitude increases, and (b) irreversible phase transitions for large-amplitude vibrations.

## 3.1 | Application of TR-PEEM

### 3.1.1 | SPP imaging

Figure 5A shows the localized surface plasmon on a rough silver grating surface, which was imaged[4] by TR-PEEM. Depending on the optical phase of the carrier ($\lambda = 400$ nm), the delay time $\tau_d$ between the pump pulse and the probe pulse can be advanced in increments of 0.33 fs or $1/2\pi$. Under optical excitation of the pump pulse, all four points will oscillate synchronously with the field ($-1/4 \times 2\pi \rightarrow 51/2 \times 2\pi$). When the driving pulse diminishes, the coherent polarization of the excitation at each point will shift to its own resonant frequency. The introduction of a phase change in the driving field will cause a delay (or advancement) in the phases of points *A*, *B*, and *D* (point *C*). Consequently, the intensity maximum will experience a delayed (or early) increase. The highlighted areas represent the locations where the intensity maxima (resulting from constructive interferences) shift due to phase discrepancy between the SP modes and the driving field within five-cycle intervals. Thus, the dynamics can be divided into three stages. (a) When the pump and probe pulses overlap at a time domain, the external light field will drive the local surface plasmon modes supported by different rough structures to vibrate in accordance with the laser carrier frequency. (b) With a time delay between the pump and the probe pulse, the different modes will have their own different vibration frequencies; thus, the vibration processes of each mode will no longer be synchronized. (c) With a sufficiently large delay between two pulses, each mode will decay exponentially. To investigate the interference phenomenon of SPPs, TR-PEEM has been used to capture both the out-of-plane and in-plane components of near-field SPP[107] in an obliquely incident femtosecond laser-excited trench. As shown in Figure 5B, interferograms were fabricated by overlapping p- or s-polarized probe pulses with either the out-of-plane or in-plane component of the SPP near field, utilizing a noncommon-linear excitation mode. The PEEM image revealed a striped shift in the in-plane interference pattern between the in-plane and out-of-plane components of the SPP field, corresponding to a 1/4 stripe period. Figure 5C shows the design of laser polarization for ultrafast spatiotemporal modulation of the preferential emission direction of SPP,[109] according to the mechanism shown in Figure 5B, which significantly improved the SPP directional extinction ratio. More importantly, the coupling state of SPP in the nanodirected coupler can be regulated by adjusting the transient polarization state of the excitation laser pulse, thereby opening up broader possibilities for future optoelectric and communication devices.

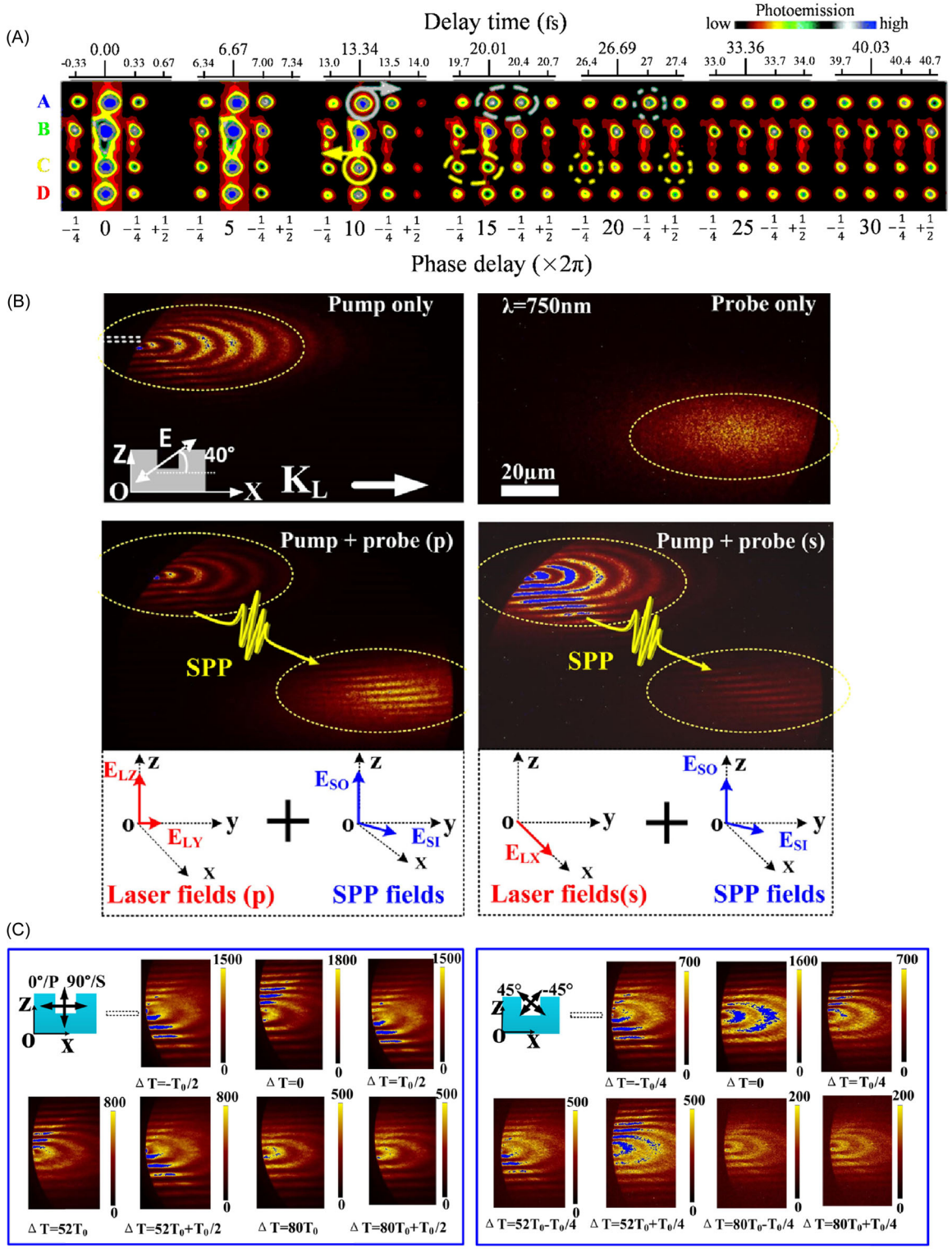


**FIGURE 5** (A) Time-resolved photoemission electron microscopy (TR-PEEM) images of the four points on a silver grating, showing the localized surface plasmons. Reproduced with permission.[4] Copyright 2005, ACS. (B) PEEM images of the noncollinear mode of a trench structure, with a shape size of 20 × 1 μm, with the two yellow circles spatially separated in the experiment. Reproduced with permission.[107] Copyright 2020, Chinese Laser Press. (C) TR-PEEM images under different time delays, where all images were captured using two 0° polarized and 90° and 45° polarized pulses. Reproduced with permission.[108] Copyright 2021, Chinese Laser Press. SPP, surface plasmon polariton.

### 3.1.2 | Ultrafast charge carrier transport

The study of ultrafast electron transport processes in heterostructures has attracted significant attention due to their promising basic science and industrial applications. Man et al.[95] from Okinawa imaged the electron transport process in semiconductor heterojunctions using the two-color pump–probe technique, as shown in Figure 6A. All images shown in Figure 6A were obtained with different detection delays and the intensity of the background signal was subtracted out, where the red color represents the carrier accumulation in InSe and the blue color represents the carrier depletion in GaAs. In general, electrons were transferred from GaAs to InSe at an early stage, leading to a rapid decay in GaAs carriers within 10 ps, as shown in Figure 6B. Between 10 and 100 ps, further electron transfer occurred from thin InSe to thick InSe due to the lower band gap in the thicker region. Finally, with time delays greater than 100 ps, the photogenerated carriers in the thicker part of InSe also gradually relaxed back to the ground state as the sample returned to the ground state. The specific energy band arrangement and carrier relaxation curves are shown in Figure 6B.

In photocatalytic reactions,[96] the transfer of charge carriers induced by photons plays a key role in determining photocatalytic efficiency. To investigate this, TR-PEEM has been used to image the electron and hole dynamics of $Cu_2O$ in photocatalysts. Figure 7A shows a series of images captured at different pump–probe time delays.[110] The anisotropic charge transfer dynamics of the particles were clearly visualized, where the charge carrier density in the [001] plane was higher than in the [111] plane, indicating that the charge carriers underwent ultrafast transfer from the [111] plane to the [001] face. Subsequently, the photoemission electron intensity slowly increased at tens of picoseconds, with decays at hundreds of picoseconds. Upon photoexcitation, the [001] facet showed negative surface photovoltage (SPV) signals, while the [111] facet showed positive SPV signals, confirming the occurrence of ultrafast inter-facet electron transfer. Theoretical and experimental findings have indicated that rapid interfacial electron transfer can occur through the establishment of a 1.7 kV/cm internal electric field from [001] to the [111] facet. As a result, the high-energy electron located at the [111] facet will undergo rapid decay within 0.1 ps after optical excitation. In contrast, the high-energy electron at the [001] facet will continue to increase until 0.1 ps, before eventually decaying with a time constant of 0.18 ps. The population of low-energy electrons at the [111] surface will remain mostly unchanged throughout the process, suggesting that the decay of high-energy electrons on the [111] facet can be primarily driven by interfacial electron transfer rather than thermalized electron relaxation or capture (Figure 7B). The study showed that the complex mechanism dominating photocatalytic charge separation could be tuned through anisotropic crystal faces and defect structures, thus providing new ideas and research methods for the rational design of photocatalysts with improved performance.

## 3.2 | Application of SUEM

### 3.2.1 | Silicon-based heterogeneous surface/interface

SUEM has been used to image the generation, transport, and complexation of charge carriers on silicon surfaces, as well as to analyze the carrier diffusion mechanisms by combining these mechanisms with the corresponding theoretical models. As an example, the hot carrier dynamics in hydrogenated amorphous silicon (a-Si:H) could be directly imaged using SUEM,[110,111] as shown in Figure 8A. To ensure the accuracy of the signal, the images were processed using two methods, either through function filtering to

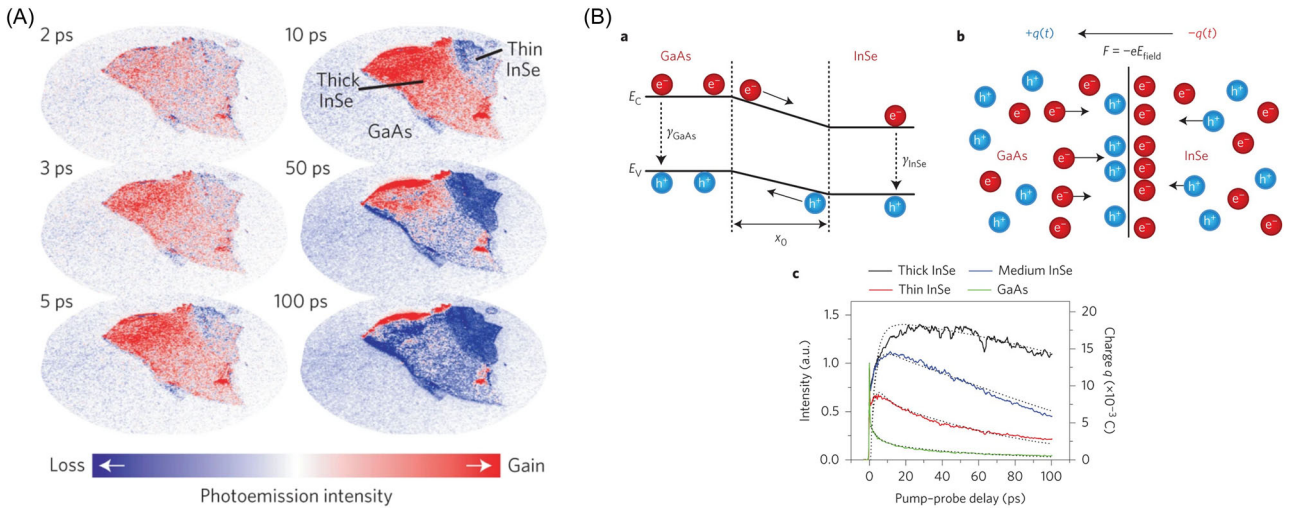


**FIGURE 6** (A) Charge carrier transfer images showing the InSe/GaAs heterostructure obtained with different delay times, where the red area represents charge accumulation and the blue area represents charge depletion. Reproduced with permission.[95] Copyright 2016, Springer Nature. (B) Quantitative model of charge separation and transfer.

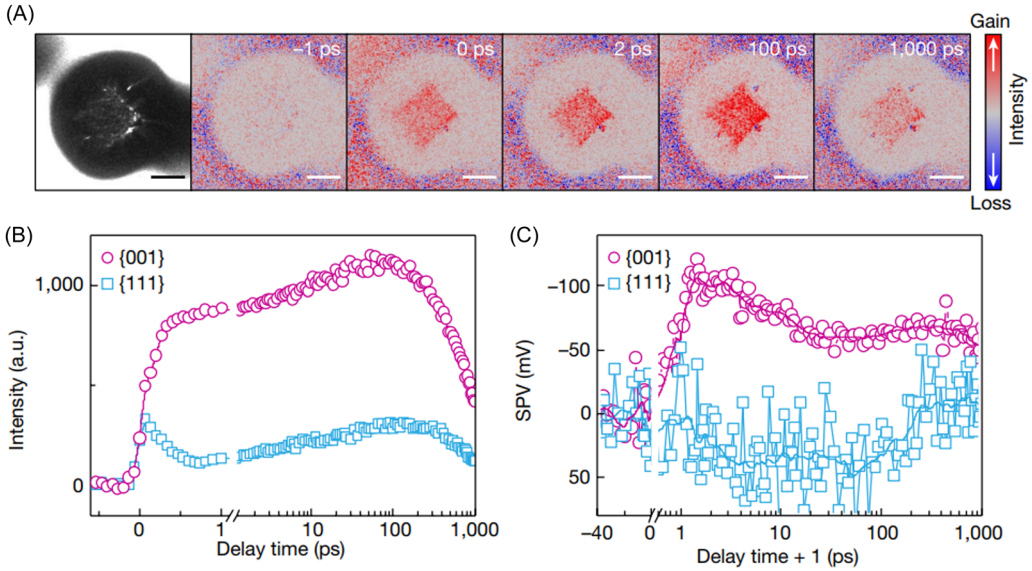


**FIGURE 7** Time-resolved photoemission electron microscopy (PEEM) images of EH-$Cu_2O$ microparticles. Reproduced with permission.[96] Copyright 2022, Springer Nature. (A) Stable and transient PEEM images of an EH-$Cu_2O$ particle obtained with different delay times, where the scale bars indicate 2 μm. (B) Relationship between the photoelectron intensity integral of the two different crystal faces of the EH-$Cu_2O$ particles and the time delay, where, to eliminate systematic errors in the experiment, signals were collected from surfaces parallel to the substrate. (C) The photoelectron spectrum was fitted, enabling the extraction of the peak shift, and this information was used to analyze the relationship between the photoelectron energy and the time delay, and smooth the points to form a solid line in the figure.

reduce spatial noise or by averaging the signal areas of multiple images. The sample surface shown in Figure 8A was excited by a pump light, leading to the generation of electron–hole pairs. As a result, the surface gradually started to brighten, forming a bright disk at a time delay of 20 ps. When the time delay ranged from 20 to 100 ps, the carriers spread laterally and the disk expanded further, while the central region started to darken at the same time. After 100 ps, the size of the disk remained essentially unchanged, while the dark contrast in the center of the disk became increasingly prominent, reaching its peak darkness near 1 ns. Through Monte Carlo transport model simulations and observations,[112] an unexpected rapid diffusion mechanism of charge carriers was revealed as shown in Figure 8D. The initial high-temperature photo-induced carriers were found to be responsible for the rapid diffusion, as also accompanied by electron and hole trapping after diffusion. The finding of this spontaneous electron–trap separation directly validated the relaxation semiconductor behavior predicted in the 1970s.[113] This work confirmed the ability of SUEM to resolve unknown problems in carrier dynamics, making it suitable for investigating different materials.

In addition to a-Si:H, SUEM has been used to study p–n junctions[62] with nanoscale interfaces (Figure 9A), with the figure showing the evolution of carriers in a p–n junction with high spatiotemporal resolution under a 1.28 $mJ/cm^2$ fluence pump. The individual p or n types, after laser excitation, showed a bright contrast. However, in the p–n junctions, the p-type part darkened rapidly after excitation, while the n-type part continued to become brighter, indicating that the p-type electrons migrated to n-type electrons. At 80 ps, carriers were observed traveling distances of up to tens of microns, at which point the density of excess carriers reached their maximum. However, the secondary electron signal of the p–n junction extended significantly beyond the depletion layer within 80 ps and the carrier density was distributed across the junction in time scales of tens of nanoseconds, contrary to the conclusion expected from plausible drift–diffusion models. After excluding the role of carrier expansion and acoustic phonons, the ballistic transport mechanism was introduced by modeling the carrier dynamics and analyzing the potential field and Coulombic interactions in the depletion region, as shown in Figure 9B,C. The fast carrier transfer was shown to be closely related to ballistic transport, and the discovery of this mechanism provided a foundation for the in-depth study of the effect of the carrier transfer path on the rectification effect of p–n junctions. Since the carrier density could be closely related to the laser fluence, the carrier behavior could be controlled by adjusting the pump fluence. The carrier oscillation effect near the depletion region of the p–n junction was also observed, after increasing the pump fluence.[100] The carrier oscillation can also form a plasma wave and the intensity of the plasma wave has been positively correlated to the value of the reverse bias voltage. The carrier transport will produce significant echoes at the interface, resulting in higher plasma oscillations in terms of frequency and faster propagation speed.

### 3.2.2 | Nanoscale structural surfaces

SUEM has also been used to resolve carrier diffusion and chirality mechanisms in new semiconductors. For example, indium gallium

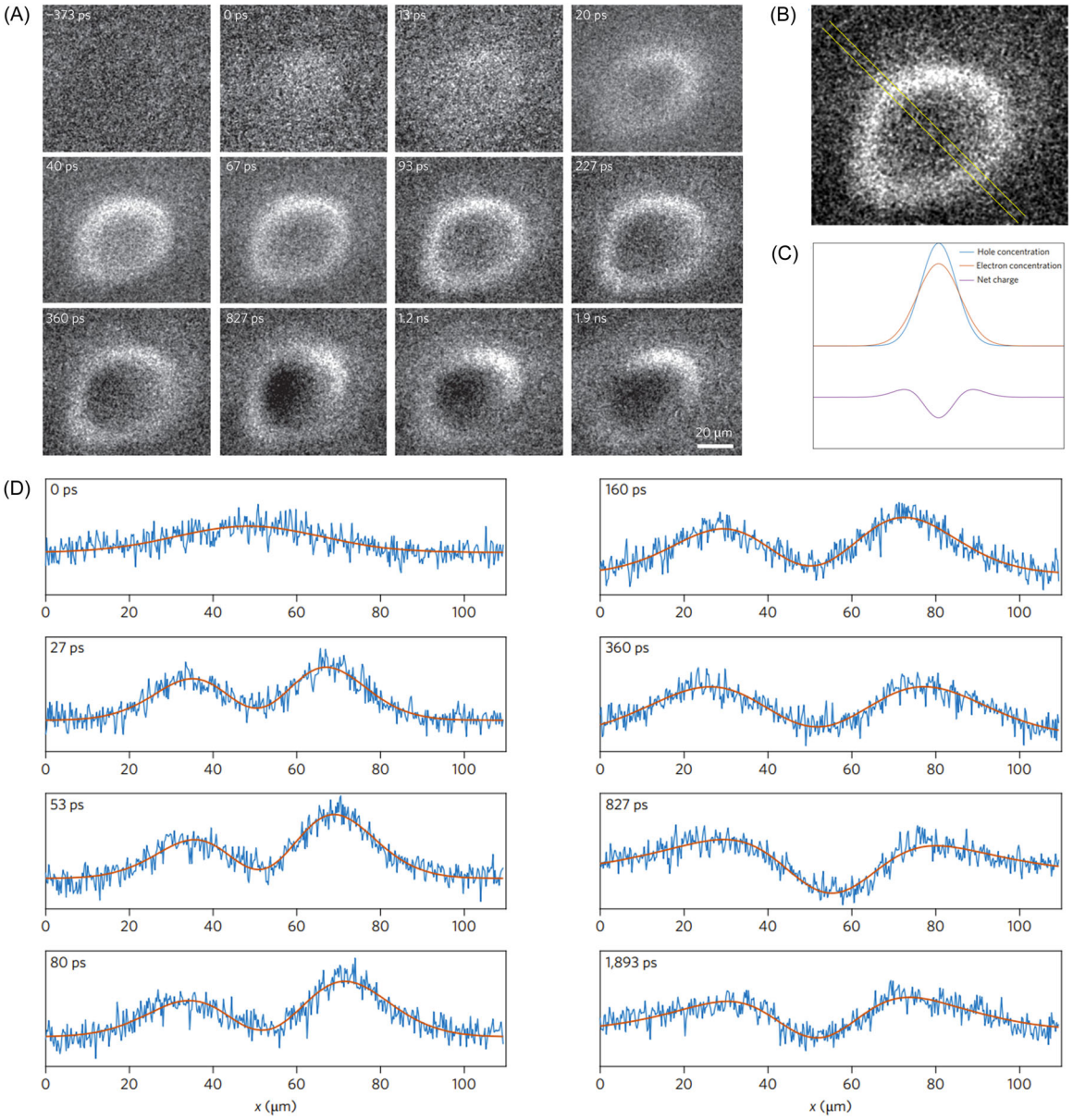


**FIGURE 8** (A) Scanning ultrafast electron microscopy images of ultrafast laser-induced hot carriers dynamics in hydrogenated amorphous silicon, where the images indicate the so-called difference images, with −680 ps serving as a reference, and the images in the datasheet were all subjected to the average process of multiple images to reduce noise. (B) The designated region, marked by yellow markers, corresponded to line-cuts. (C) Illustration explaining the experimental findings, showing the spatial distributions of the hole and electron concentrations represented by blue and orange lines, respectively, and the purple line representing the different charge distributions between the hole and electron distributions. (D) An unexpected rapid diffusion mechanism of charge carriers. Reproduced with permission.[110] Copyright 2017, Springer Nature.

nitride (InGaN) nanowires (NWs) have been widely used as optoelectronic devices, but the energy conversion efficiency remains limited by various factors and their origin is not clear when applied as devices. As shown in Figure 10A, the ultrafast evolution process of secondary electrons was imaged using SUEM and the intensity distribution pattern of secondary electrons at the positive and negative delay times was compared.[81] Above −300 ps, no significant change was observed in the signal region contrast, which indicated that the carriers excited by the pump light of the previous cycle fully recovered before the next cycle of pump pulse arrived. The illustration also shows the dynamics of electron diffusion by comparing the brightness changes at the center and edge of the pump spot, with the hole combination or Auger combination identified as the main mechanism of nonradiative energy loss, and was also consistent with the numerical simulation results. In this case, the surface state-dependent Shockley–Read–Hall recombination was regarded as the main electron–hole recombination mode, rather than bimolecular electron–hole complexation. Based on the above results, a strategy for passivation of surface defects in NWs by octadecyl thiol was proposed.[99] As shown by the time-resolved SE image in

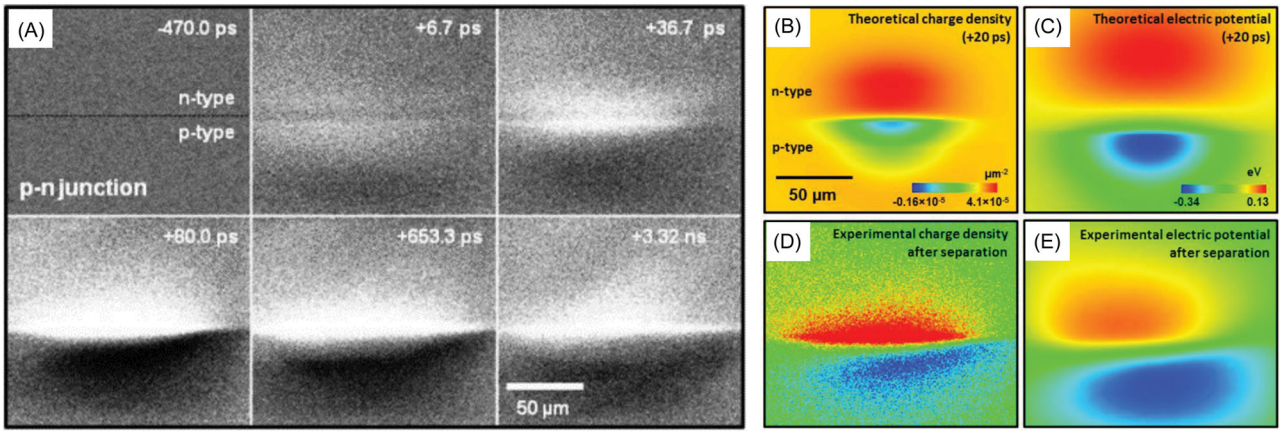


**FIGURE 9** (A) A sequence of contrast images, with the bright contrast representing high electron density and the dark contrast representing high hole density, relative to the signal observed at negative time. (B) Simulation results for a net charge density of +20 ps. (C) Direct calculation of the Coulombic interactions between the separated carriers. (D) Experimental image of the junction provided, showing the mirrored charge densities in the n- and p-type regions following charge separation. (E) Dynamic potential map obtained by direct calculation. Reproduced with permission.[62] Copyright 2015, AAAS.

Figure 10B, NW carrier recombination after passivation was greatly reduced (from 40% to 15%). The illustration at the top of Figure 10B, which represents the cross-section of the NWs after passivation, showed that passivation did not lead to any topographic changes. The middle illustration shows a time-resolved SE intensity kinetic curve and the difference between the carrier dynamics before and after passivation. This served as an outstanding result of the high time-resolved electron beam imaging technique for device optimization, which could directly enhance the luminescence performance of the InGaN/GaN quantum devices. In addition, the ultrafast secondary electron images of the Si-doped InGaN/GaN NW dynamics showed that the doping of Si could affect the surface carrier dynamics of InGaN NWs,[114] as shown in Figure 10C. Similar to the images in Figure 10A, no significant change in the signal region contrast was observed with a negative time delay, indicating complete recombination of the carriers while the next cycle of pump pulse arrived. With an increase in the Si doping concentration, the growth of the SE signal on the doped NW surfaces slowed down in the first 100 ps and decayed faster after 100 ps. At this time, the defect state energy level formed by doping interacted with the free electrons and localized electrons to reduce the electron escape rate by scattering. This led to the energy loss presented in the dark contrast, which subsequently affected the photoconductivity of the NWs. The above results showed that SUEM can play an important role in carrier dynamics and device electronic properties, paving the way for further performance optimization of devices.

### 3.2.3 | GaAs/CdTe single crystals

In optoelectronic applications, defects will hinder carrier transport and affect device performance. Therefore, defect-free single-crystal semiconductors are considered to be highly promising materials,[111,115] making it critical to study the carrier dynamics of single crystals. As shown in the secondary difference electron images of the GaAs single-crystal surface in Figure 11, the doping effect on carrier dynamics was explored. As shown in Figure 11A, dark contrast was observed for both negative and positive time delays, and the extraction of the central SE intensity of the undoped and doped SEs images was plotted, as shown in Figure 11B. The most significant doping-dependent enhancement at time zero occurred in n-type GaAs (110) for specific reasons. In n-type GaAs, minimal presence of electrons near the donor energy level close to the conduction band was observed, while the density of states was comparatively high. As a result, when absorption occurred, these electrons were efficiently promoted to the conduction band, leading to a pronounced enhancement effect. However, in p-type GaAs, the photoexcited electrons were positioned further away from the vacuum level of GaAs than the n-type counterpart, and this disparity originated from the donor energy level located at the proximity of the valence band maximum in p-type GaAs. As shown in Figure 11B, a clear segmental decay was observed according to the carrier decay rate, indicating that a dark contrast signal in the n-type GaAs decayed extremely rapidly within 100 ps, while after 100 ps, the dark contrast signal decayed slowly. Considering nanosecond-scale carrier dynamics, the dark contrast signal for the undoped GaAs decayed only 50% between 100 and 2500 ps (Figure 11B). In n-type GaAs, this decay rate was further reduced to about 30%. After exponential fitting, GaAs (110) showed a time constant $t_1$ of the order of nanoseconds, while in n- and p-type GaAs, time constants $t_2$ on the order of picoseconds were observed at 207 ± 131 and 39 ± 17 ps, respectively. The carrier lifetime at this stage in n-type doping was much greater than the p-type doping. This was mainly because the effective cross-sections of the SEs scattered by the conduction band electrons were much larger than that of SEs scattered by valence band electrons, resulting in a lower probability of SE emission, thus creating a dark contrast.

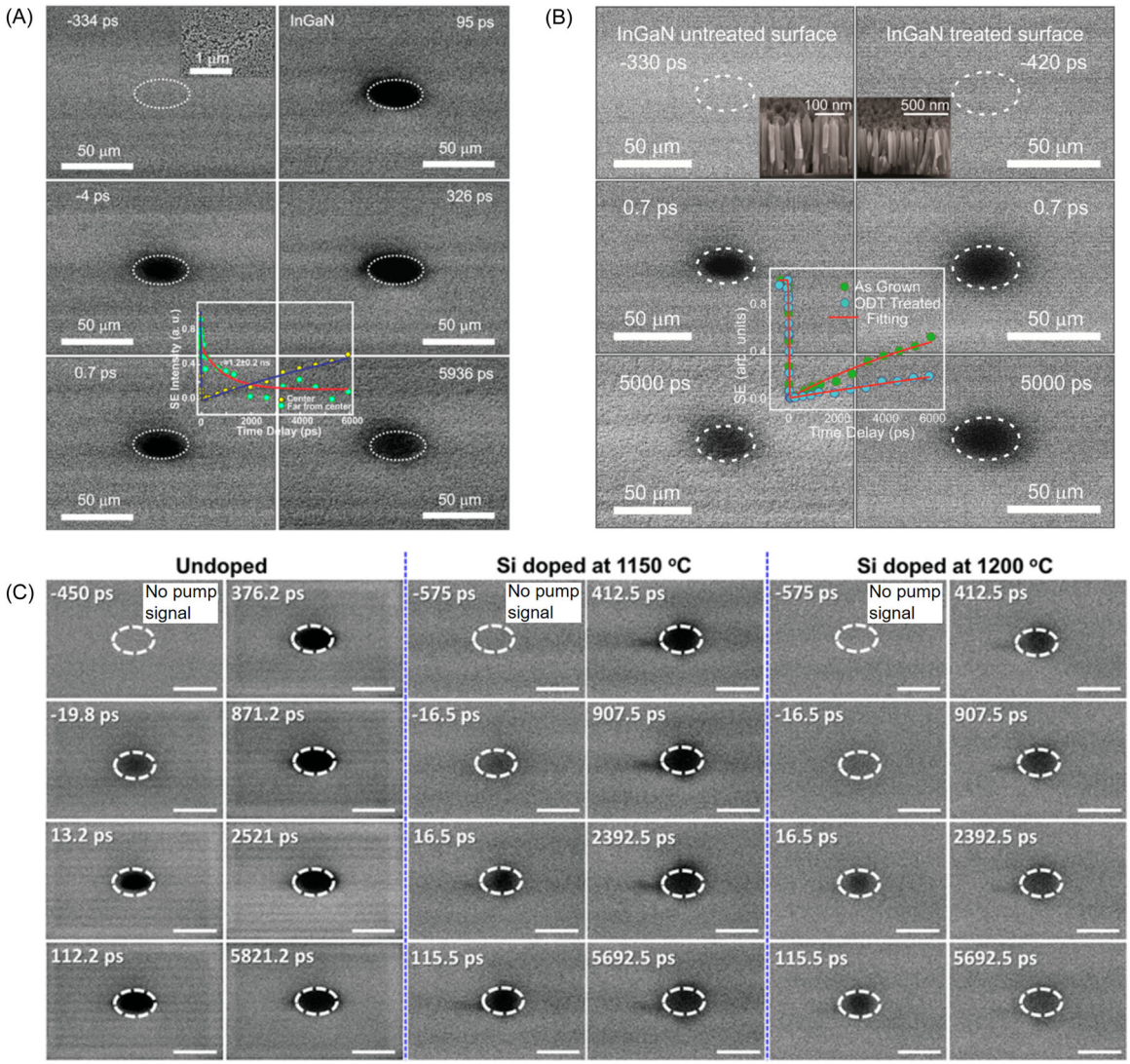


**FIGURE 10** (A) Time-resolved secondary electron image of the indium gallium nitride (InGaN) nanowires (NWs), dotted at the spot position, with a long axis of about 40 μm. Reproduced with permission.[81] Copyright 2016, Wiley-VCH. (B) Time-resolved secondary electron (SE) image of InGaN NW before and after surface passivation, with the illustration showing the considerable difference in carrier recovery rate before and after passivation. Reproduced with permission.[99] Copyright 2016, Wiley-VCH. (C) Time-resolved SE image of the silicon surface after background extraction, with a pump excitation wavelength of 515 nm. The scale bar indicates 50 μm. Reproduced with permission.[114] Copyright 2018, ACS.

The surface orientation of the crystal is another crucial factor, alongside doping, that will influence the carrier properties of the material. Figure 11C shows the significant impact of surface orientation and termination on the photoexcited carrier dynamics and carrier diffusion length of CdTe single crystals,[101] indicating that the charge carriers diffused in the CdTe (110) surface direction within 6 ns for nearly 80 μm (inset), where the high diffusion coefficient of 40 000 $cm^2/s$ indicated an extremely low density of trap states on the CdTe (110) surface side. Gradually, the diffusion length and coefficient on the CdTe (111) showed a sharp decrease compared to CdTe (110). In contrast, the photo-induced carriers were easily trapped on the CdTe (211) surface orientation with a trapping time greater than 200 ps, which was due to the presence of defect states caused by the formation of an oxide layer on the surface. Use of S-UEM to study the carrier dynamics in single crystals is critical for revealing the key factors to enhance the quality of single crystals.

## 3.3 | Application of UTEM

### 3.3.1 | Electron–lattice dynamics of typical two-dimensional materials

TMDs are materials with potential applications in tunable opto-electronic devices due to their electronic properties of strain sensitivity. Therefore, understanding their strain properties has become especially important. By conducting ultrafast electron diffraction imaging, evidence has been found for the presence of

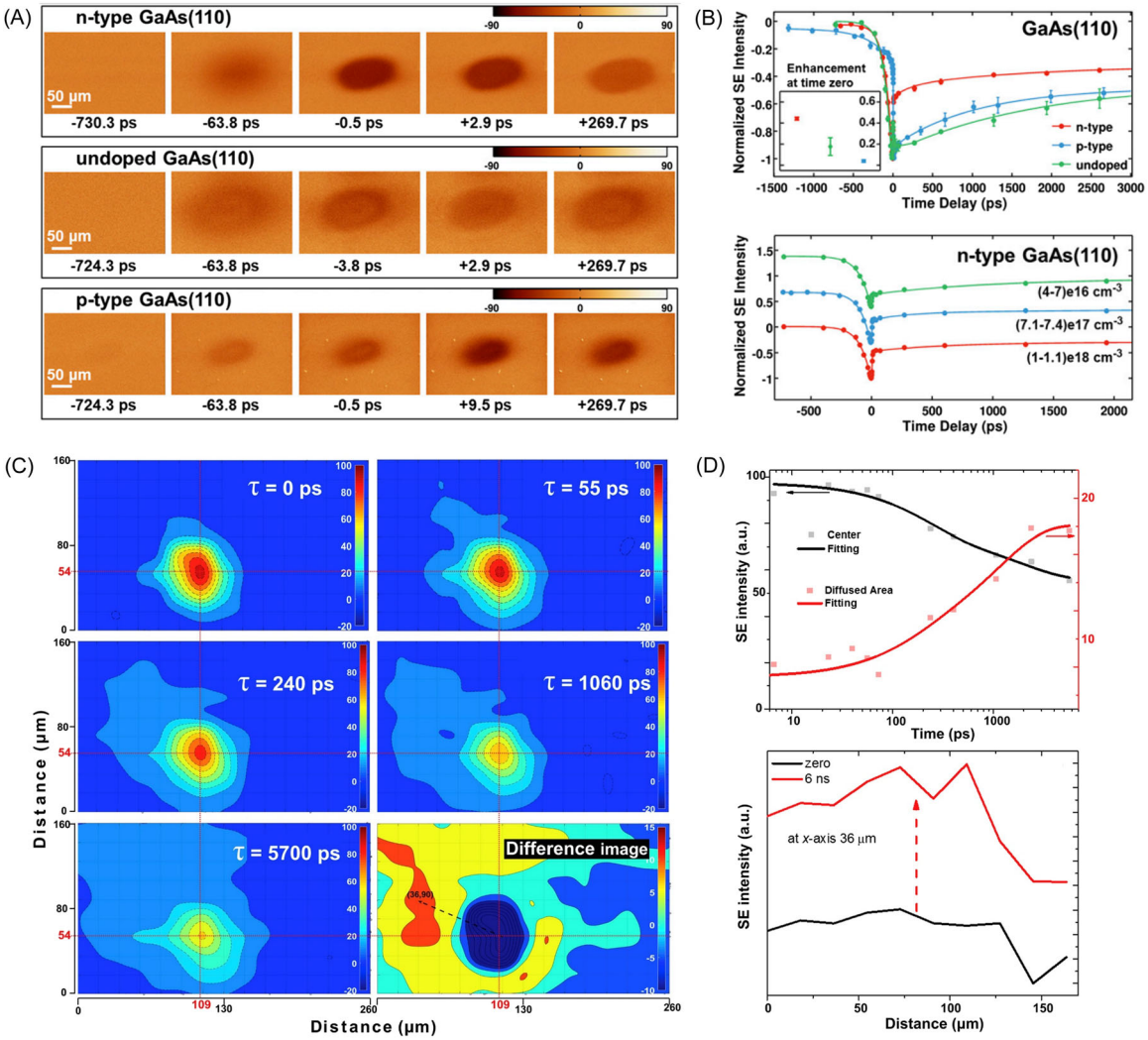


**FIGURE 11** (A) Secondary electron (SE) difference images obtained from GaAs (110) with noted doping types. Reproduced with permission.[111] Copyright 2021, ACS. (B) Carrier concentrations in n-type, p-type, and undoped GaAs (110) and noted n-doped GaAs (110). (C) Time-resolved secondary electron image results of CdTe (110), Reproduced with permission.[101] Copyright 2019, Elsevier; all images were treated with background reduction and pseudo-color to reflect the secondary electron signal intensity distribution, with the arrows in the pseudo-color plot indicating the carrier diffusion direction, pointing from the center of the pump light excitation to the region with the greatest change in secondary electron signal intensity. (D) Extract of the secondary electron intensity of the region with the greatest change in the center of the pump spot and the region with the greatest intensity change for fitting the carrier dynamics behavior of the crystal facet.

delays between different excitation modes.[105] The bright-field image shown in Figure 12A was taken along the ki → ∠ [001] = 40° crystal section, 14 ps before initial contrast, and the two specific bend contours analyzed in Figure 12B are labeled 1 and 2 in Figure 12A. The spatial fast Fourier transform of this region of interest yielded two discrete oscillation frequencies of 56.7 and 63.3 GHz, as shown in Figure 12C and D, respectively. These two signals possibly converged at the edge of the step, forming a 60 GHz signal. On analyzing the motion state of a single target region, each region was found to have a specific oscillation pattern related to the thickness of the region and the surrounding conditions, as shown in Figure 12C,E. Thus, this suggested a combination of changes in the initial pulse structure along the *c*-axis direction, with an increase in the step edge and step-edge $MoS_2$ layer motion at the edge of the degree of freedom, and propagation as an in-plane strain wave at longitudinal velocities (2.6–2.9 nm/ps observed).

The optical excitation of TMDs is known to produce transient strain effects; however, the associated acoustic–phonon modes at low frequencies (tens of GHz) within and between the layers remain unexplored, especially with respect to defects prevalent in these types of materials. When using UTEM to probe the nanoscale-softened individual surface steps[116] in Figure 12F–H, a large degree of softening (lower frequency) at the step was found, which was thickness dependent. The strain-induced frequency modulation properties also extended from tens of nanometers to the discontinuous atomic scale. This effect was caused by anisotropic bond expansion and photo-induced incoherence. The magnitude and spatiotemporal extents of

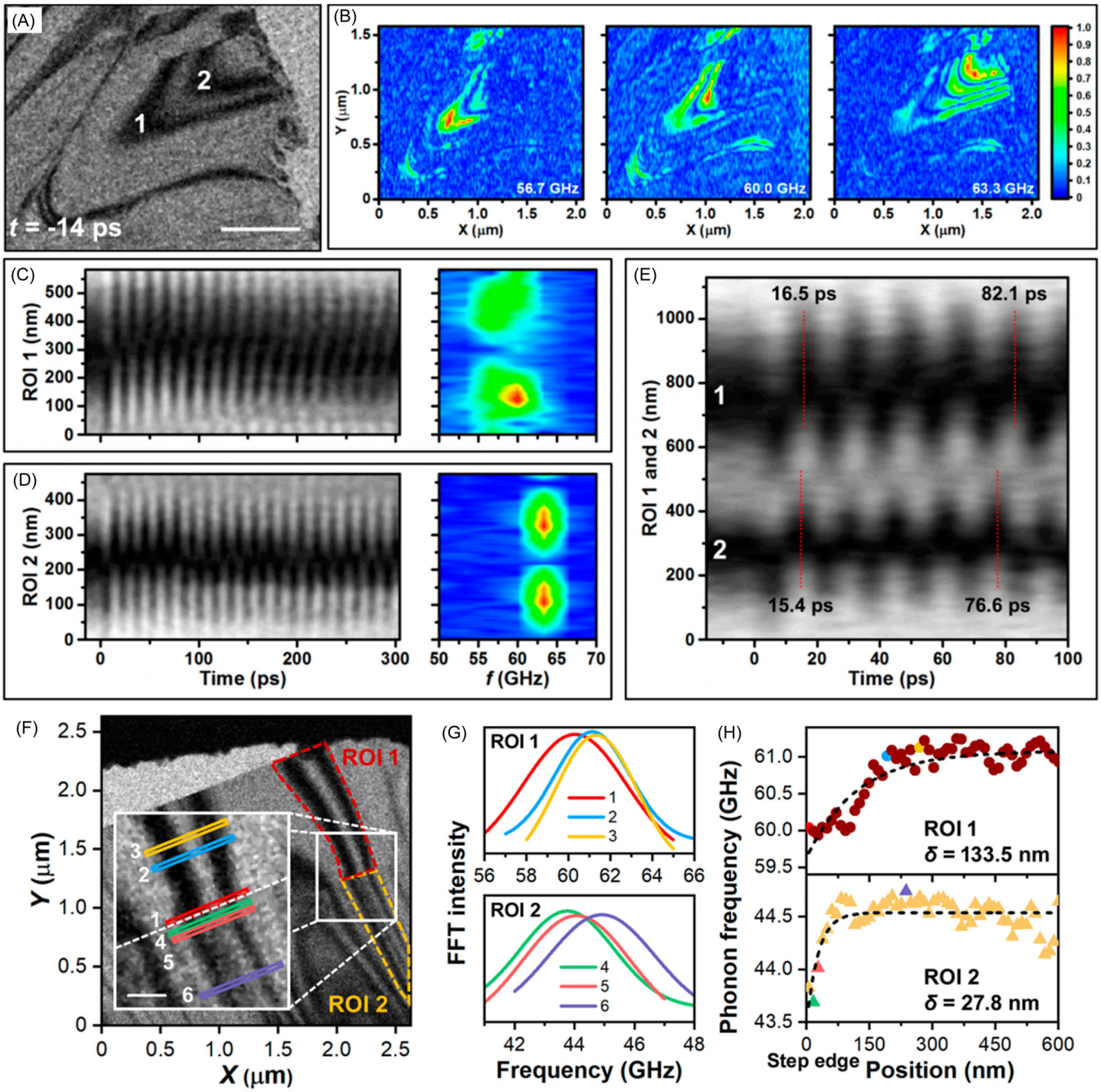


**FIGURE 12** Few-layer dephasing behavior of stress waves between $MoS_2$ layers. Reproduced with permission.[116] Copyright 2021, ACS. Reproduced with permission.[105] Copyright 2019, ACS. (A) Ultrafast transmission electron microscopy (UTEM) bright-field image with a negative time delay (−14 ps), where the ruler in the picture represents 500 nm. (B) Spatial distribution of the oscillating frequency intensity in the three regions in (A), which were 56.7, 60.0, and 63.3 GHz, respectively. (C, D) STCP of the two regions marked in (A). (E) STCP of regions 1 and 2 in (A) with a 100 ps time delay. (F) UTEM image of a 2H-$MoS_2$ thin nanosheet, showing the regions of interest (ROIs) extracted by phonon oscillation, where the ruler represents 150 nm. (G) Frequency after FFT transformation at a specific position in (A), where the degree of frequency shift at different positions near the step could be determined; and (H) phonon position correlation frequency in each region of interest, with the position relative to step size and the step size set to 0 nm. FFT, fast Fourier transform; STCP, space-time contour plot.

softening were quantitatively described by a finite element transient deformation model. These results revealed novel insights into the response of the underlying nanoscale structure in ultrafast laser-exciting low-dimensional materials, illustrating the defect behavior affecting these materials.

### 3.3.2 | Reversible phase transition processes

Significant progress in charge density waves (CDW) has been made in recent years in quasi-two-dimensional systems.[117,118] However, the correlation of charge, spin, and lattices in strongly correlated systems

makes it difficult to resolve the effects of different orders on the material properties. The mechanism of CDW formation also remains unclear. By introducing a customized ultrafast dark-field electron microscope with an aperture array, the order parameter of the structural phase transition of a typical CDW system could be obtained.[103] Figure 13A shows that as the continuous laser intensity increased, the insulating (IC) domains nucleated and grew close to the center of the film, until the domains almost filled the circular hole. Decreasing the laser intensity led to a decrease in the switching area. The subsequent simulations also illustrated that the temperature distribution was the main reason for phase transition under steady-state excitation. The time-resolved dark-field image shown in Figure 13E revealed the presence of nonuniform suppression of image intensity following the temporal interval between the pump laser and probe electron pulses. Within 2 ps, distinct regions with well-defined boundaries started to emerge, indicating clear contrast between the bright and dark areas. Over the course of 100 ps, these dark regions experienced slight expansion, accompanied by further contrast sharpening. Eventually, the size of these regions diminished, and a uniform contrast was restored across the material after a few nanoseconds. To understand the first-order phase transition from the nonconducting (NC) to IC phases, researchers utilized the Ginzburg–Landau model to simulate the ordered covariance and three-dimensional dynamics of the electron and lattice temperatures. The study captured the symmetry-breaking nature of the phase transition and its effect on the material, indicating that a sufficient excitation density caused the order parameter to quickly relax to a minimal value of the IC potential within the electron–lattice coupling

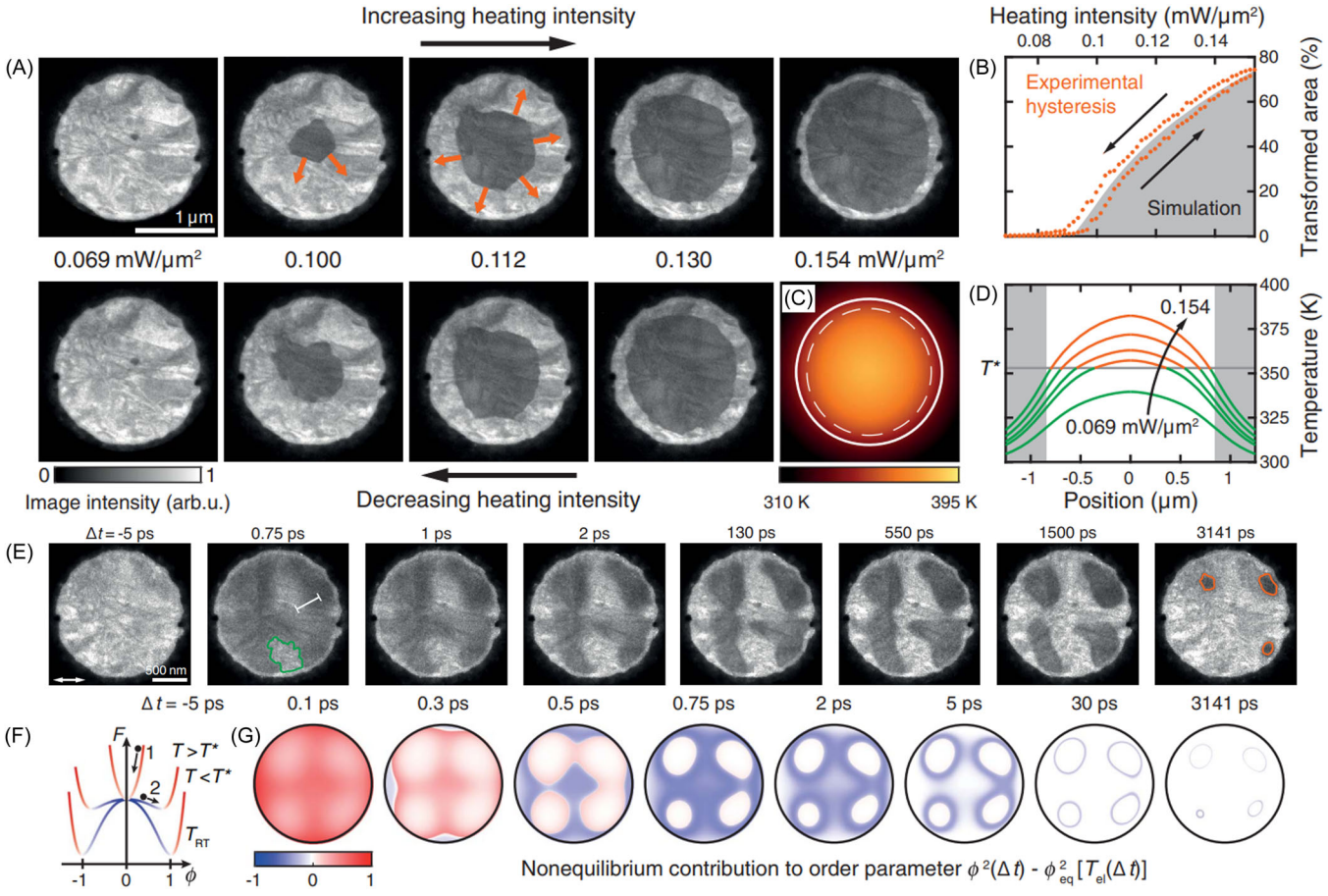


**FIGURE 13** (A) Steady-state dark-field image acquired when the sample was excited by continuous light, where the first row represents the dark-field image scanned when the laser intensity increased and the second row represents the dark-field image scanned when the laser intensity decreased, with the dark area in the center of the image representing the area where phase transition occurred. Reproduced with permission.[103] Copyright 2021, AAAS. (B) Relationship between the percentage of the phase transition region and scanning temperature extracted from (A), indicating a clear hysteresis feature. (C) Spatial distribution of temperature at 0.154 mW/mm$^2$ laser flux calculated by steady-state heat transfer. (D) Radial distribution of sample temperature at each laser intensity in (A) when the heating spot was considered a Gaussian distribution, which also identified the critical phase transition temperature. (E) Time-resolved dark-field micrograph based on ultrafast transmission electron microscopy with an excitation flux of 2.6 mJ/cm$^2$ and excitation using linear polarized light. (F) Degree of free-energy distribution corresponding to the electron temperature calculated by density functional theory. (G) Deviation of the squared order parameter from its local equilibrium value $f2$ eq (red and blue regions denote the order parameters that were larger and smaller, respectively, than at the free-energy minimum).

time (point 1 in Figure 13F). The evolution of four distinct white patches closely followed the reshaping of the potential on the thermal diffusion timescale. Conversely, in regions with weaker excitation, near the flat potential just below the phase transition temperature, transient bursts of the NC phase occurred, which dissipated within a few picoseconds (point 2 in Figure 13F). In summary, this study provided valuable insights into the high-resolution spatiotemporal evolution of the CDW domains, elucidating the dynamics, stabilization, and relaxation pathways of the CDW domains following optical excitation. The research also highlighted the significant differences in domain patterns that can arise under continuous wave and pulsed illumination conditions.

Previous studies have also investigated magnetodynamic transitions using Lorentzian MnNiGa.[13] As shown in Figure 14, in one study, four distinct magnetic states were observed and their respective atomic spin models were illustrated. The time constants of the second process (2–3) and the third process (3–4) could be estimated by fitting $\sigma$ with empirical double-exponential functions, yielding $\tau_{2-3} = 3 \pm 0.5$ ps and $\tau_{3-4} = 12 \pm 1$ ps, respectively. The study found that under femtosecond laser excitation, a dramatic change in magnetic domains was observed in the range of 10–100 ps, and the line profiles showed three successive magnetic transitions: a streak-like contrast generated by the magnetic helix disappeared very quickly (1.3 ps), partial recovery (1.3–8 ps), and complete disappearance (8–40 ps). Four magnetization states were involved: the initial magnetization state, the magnetization state after rapid demagnetization, the partially recovered magnetization state, and the paramagnetic state. Based on the three-temperature model, which was used to calculate the temperature of the electron, spin, and lattice systems with time, the results showed that the temperature of the electron and spin increased rapidly after photoexcitation, leading to rapid disruption of the magnetic order and a change in magnetic domains.

### 3.3.3 | Irreversible phase transition process

An intense laser light interacting with a material will cause the amplitude of the atomic vibrations to increase, causing the sample to melt and undergo ultrafast phase transition from an ordered crystalline to a disordered liquid state.[106]

According to molecular dynamics simulations, this order-to-disorder transition can typically be divided into two modes: heterogeneous melting at low energy density, which is often caused by lattice thermal conductivity, occurring within hundreds of picoseconds, and homogeneous melting at high energy density, which is facilitated by electron–lattice coupling and can occur from within a few picoseconds to tens of picoseconds. Figure 15 shows the material melting process under different energy ablation values using ultrafast electron diffraction.[106] At the highest energy density of 1.17 MJ/kg (Figure 15A–D), a significant decrease in diffraction spot intensity occurred at a delay of 2 ps. When the delay was increased to 7 ps, the diffraction spot intensity representing the solid state was lower than the diffraction ring intensity representing the liquid phase, indicating the formation of a disordered state. At 17 ps, the solid state completely disappeared, leaving only the diffraction ring. When the energy density decreased to 0.36 MJ/kg (Figure 1E–H), both the diffraction spots representing the solid state

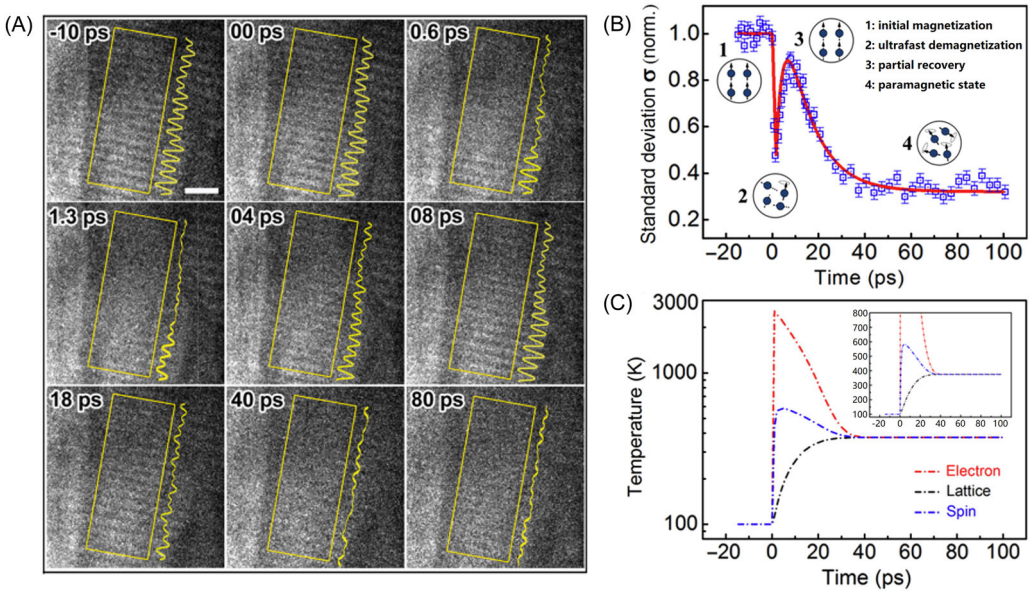


**FIGURE 14** High-spatiotemporal resolution ultrafast transmission electron microscopy images of Mn–Ni–Ga with an initial temperature of 100 K, where all images were exposed for a long time to improve the signal-to-noise ratio. Reproduced with permission.[13] Copyright 2021, APS. (A) Images taken with different time delays, where the line contours of the yellow rectangular area were superimposed to form a yellow curve next to it, which was used to characterize the phase transition characteristics, and the scale bar represents 500 nm. (B) Standard deviation σ at different time delays. (C) Evolution of temperature over time in the three electron, spin, and lattice systems under the three-temperature model.

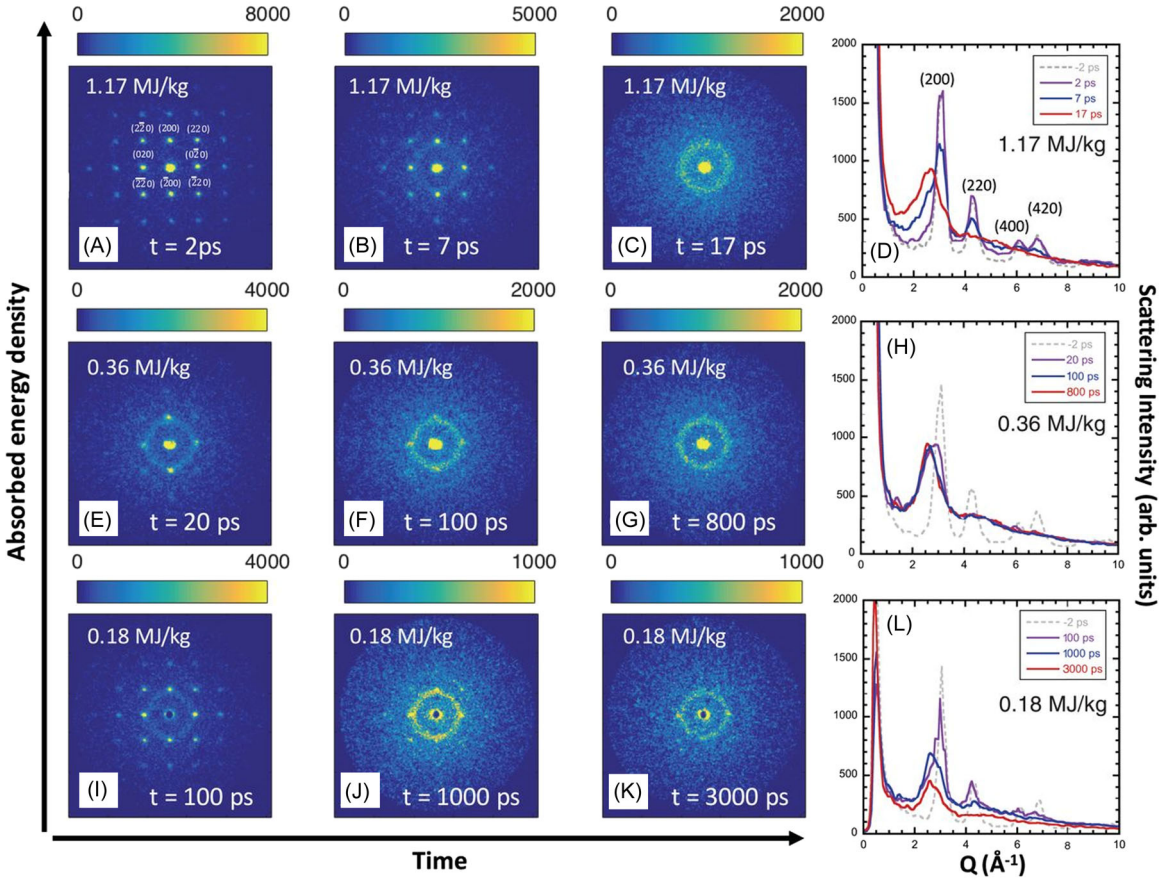


**FIGURE 15** Ultrafast electron diffraction pattern of gold film melting. Reproduced with permission.[106] Copyright 2018, AAAS. As the energy density increased, the film underwent transformation from heterogenous to homogenous melting. (A–C) Snapshots of diffraction patterns at 2, 7, and 17 ps pumped at $e$ = 1.17 MJ/kg, with the radially averaged lineouts shown in (D). (E and F) Snapshots of diffraction patterns 20, 100, and 800 ps pumped at $e$ = 0.36 MJ/kg, with the radially averaged lineouts shown in (H). (I–K) Snapshots of diffraction patterns 100, 1000, and 3000 ps pumped at $e$ = 0.18 MJ/kg, with the radially averaged lineouts shown in (L).

and primary diffraction rings from the liquid gold were visible at 20 ps, and this coexistence of the two diffraction features persisted for a long time: up to 800 ps. This delay was significantly longer than the electron–lattice thermal equilibrium time of the gold film, demonstrating the presence of heterogeneous melting over an extended period. Under lower irradiation of 0.18 MJ/kg (Figure 15I–L), the diffraction spots representing the solid phase persisted for an extremely long time, remaining in a solid–liquid coexistence state even at 3000 ps, indicating an incomplete melting process. The ultrafast electron imaging method could not only be used to assess the metal ablation behavior but also to observe the dynamics of particles in a solution.

With the integration of a vessel in UTEM, the ultrafast process in liquid environments has been detected, as shown in Figure 16. Laser irradiation can also induce agglomeration, crosslinking, and fusion between gold nanoparticles in aqueous solutions,[104] with the agglomeration, crosslinking, and fusion of nanoparticles basically proceeding along the polarization direction of the laser. Studies have also found that the above light-induced agglomeration, crosslinking, and fusion between the gold nanoparticles and fusion-irreversible reaction kinetic processes occurred in the nanosecond delay range. To better understand the kinetic mechanism of the above ultrafast reaction, the liquid environment femtosecond electron flash imaging technique, liquid environment femtosecond time-resolved electron energy loss spectroscopy, and the energy filtering imaging technique were developed. The transient crescent-shaped SPP around the gold nanoparticles in solution under femtosecond laser excitation was observed for the first time. The local electromagnetic field was found to be distributed along the polarization direction of the laser, and the intensity increased linearly with laser fluence, indicating that agglomeration among the gold nanoparticles was due to femtosecond laser-induced SPP oscillation. Under higher laser fluence irradiation, ultrafast cross-linking and even fusion reactions would occur due to the transient strong photothermal effect on the surface, resulting in the formation of larger nanoparticles.

## 4 | SUMMARY

In summary, developments in laser technology and electron microscopy have resulted in the rapid progress of ultrafast electron imaging and the discovery of numerous new phenomena and

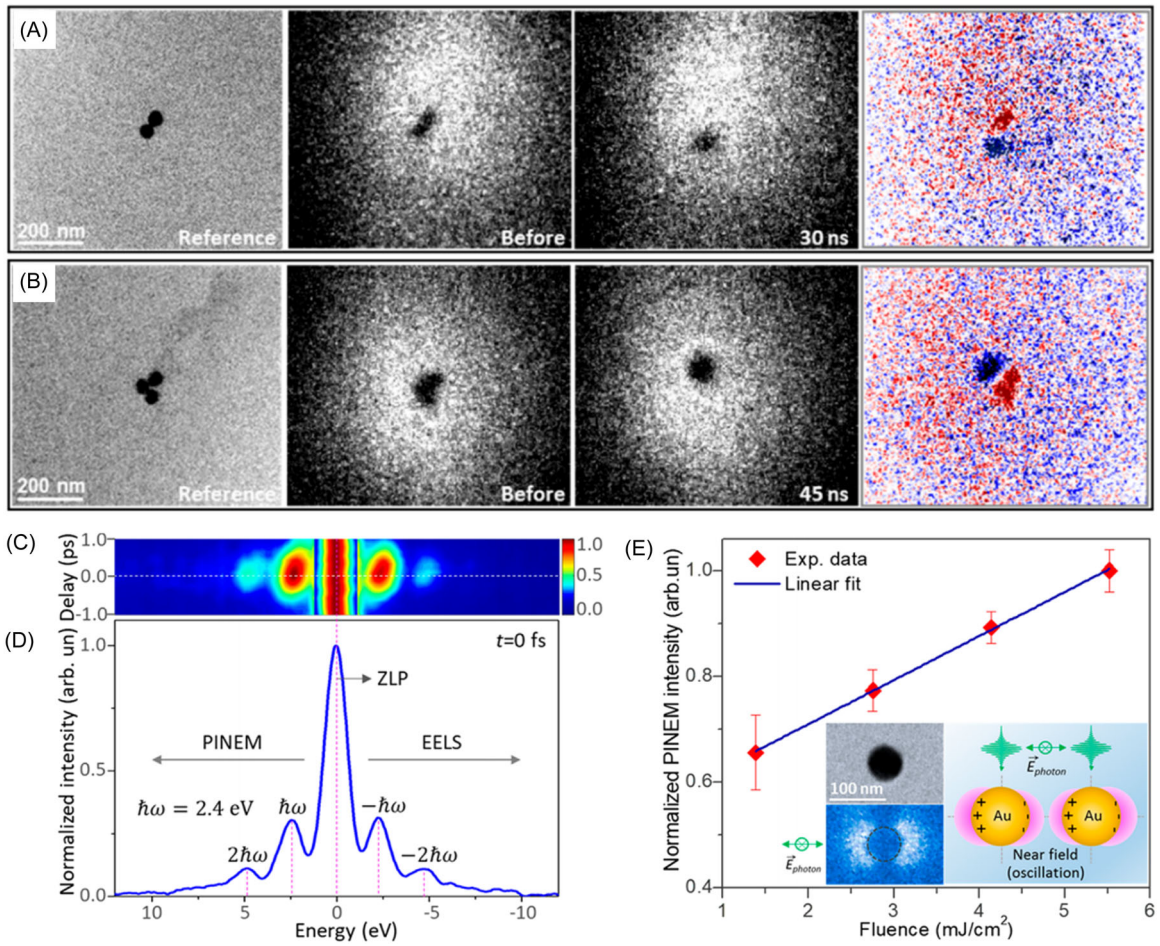


**FIGURE 16** (A) and (B) Single-pulse ultrafast electron imaging of nanosecond fusion dynamics for two- and three-AuNP clusters. Reproduced with permission.[104] Copyright 2018, ACS. (C) Time-resolved relative electron energy spectrum including the PINEM and EELS of AuNPs in liquid with an excitation fluence of 2.8 mJ/cm$^2$. (D) PINEM electron energy spectrum at $t$ = 0 fs. (E) Relationship between laser fluence and the PINEM signal of AuNPs in an aqueous solution, where the plot represents the relative intensity of the first peak on the gain side, illustrating how the PINEM signal varied with different laser fluences. EELS, electron energy loss spectroscopy; PINEM, photon-induced near-field electron microscopy.

mechanisms at the electron–atom level. This has significantly contributed to research in fundamental physics, chemistry, and materials, with important applications in electronic devices and photocatalysis. This review article focused on the principles and applications of three typical ultrafast electron imaging methods, namely, TR-PEEM, SUEM, and UTEM. By analyzing the principles of these techniques, we determined that the generation and acquisition of ultrafast electron beams serve as the key point in ultrafast electron imaging, and their imaging characteristics govern the following application areas:

(1) TR-PEEM can acquire the spatial distribution of surface photoelectrons, resolving the electron energy distribution, and revealing the action mode of SPP at different stages to verify the serial modulation mechanism. It has also shown heterogeneous interfacial electron transfer induced by the energy band gradient, with ultrafast electron transport caused by the built-in electric field in single-crystal materials through the change in photoelectron intensity distribution.

(2) SUEM can collect electrons from surface spillover under ultrafast electron beam excitation, providing higher spatial resolution. For example, the high-temperature-induced fast carrier diffusion in silicon materials and ballistic motion at the silicon p–n junction interface can be resolved. Moreover, the important effects of defect modification and energy band modulation on the carrier properties of semiconductor NWs have been illustrated. The key influencing factors of the carrier dynamics of single crystals, such as defects, doping, and the surface orientation, have been represented.

(3) UTEM can directly acquire images by collecting the electron beam and transmitting the sample, with multiple imaging modes. For example, in real space mode, it can reveal the stress propagation and lattice softening in TMDs and elucidate the specific process of martensitic phase transformation of metallic materials from a microscopic perspective. In the inverted space, it

can image the lattice melting and crystallization processes under destructive excitation.

Although it is difficult to cover all research on ultrafast electron imaging, this review may serve as a reference for researchers in related fields when studying ultrafast electron imaging. We believe that advances in instrumentation will lead to further developments in ultrafast electron imaging, with higher spatial and temporal resolution. Novel optical field modulation techniques may induce more new processes in materials and the introduction of other energy fields will likely expand the application areas of ultrafast electron imaging. The boom in ultrafast electron imaging technology will also play a more significant role in both future scientific research and engineering applications.

## ACKNOWLEDGMENTS

The manuscript was written through the contributions of all authors. All authors have given their approval to the final version of the manuscript.

## CONFLICT OF INTEREST STATEMENT

The authors declare no conflict of interest.

## DATA AVAILABILITY STATEMENT

Data will be made available on request.

## ORCID

*Lan Jiang* http://orcid.org/0000-0003-0488-1987

## REFERENCES

1. Chi Z, Chen H, Chen Z, Zhao Q, Chen H, Weng YX. Ultrafast energy dissipation via coupling with internal and external phonons in two-dimensional $MoS_2$. *ACS Nano*. 2018;12(9):8961-8969.
2. Jiang L, Wang A-D, Li B, Cui T-H, Lu Y-F. Electrons dynamics control by shaping femtosecond laser pulses in micro/nanofabrication: modeling, method, measurement and application. *Light Sci Appl*. 2018;7(2):17134.
3. Trovatello C, Miranda HPC, Molina-Sánchez A, et al. Strongly coupled coherent phonons in single-layer $MoS_2$. *ACS Nano*. 2020;14(5):5700-5710.
4. Kubo A, Onda K, Petek H, Sun Z, Jung YS, Kim HK. Femtosecond imaging of surface plasmon dynamics in a nanostructured silver film. *Nano Lett*. 2005;5(6):1123-1127.
5. Zhan N, Jia J, Guo B, Jiang L, Wang L, Zhang Q. Efficiency enhancement by transient electron dynamic control in shaped femtosecond laser fabrication of metals. *Appl Surf Sci*. 2022;603:154441.
6. Guo B, Sun J, Lu Y, Jiang L. Ultrafast dynamics observation during femtosecond laser-material interaction. *Int J Extreme Manuf*. 2019;1(3):032004.
7. Wang D, Wei S, Yuan X, et al. Ultrafast imaging for uncovering laser-material interaction dynamics. *Int J Mech Syst Dyn*. 2022;2(1):65-81.
8. Garming MWH, Weppelman IGC, Lee M, Stavenga T, Hoogenboom JP. Ultrafast scanning electron microscopy with sub-micrometer optical pump resolution. *Appl Phys Rev*. 2022;9(2):021418.
9. Zaum C, Osterloh N, Darkins R, Duffy DM, Morgenstern K. Real-space observation of surface structuring induced by ultra-fast-laser illumination far below the melting threshold. *Sci Rep*. 2021;11(1):13269.
10. Ning Z, Lian Y, Jiang L, Sun J, Wu S, Wang F. Femtosecond laser-induced anisotropic structure and nonlinear optical response of yttria-stabilized zirconia single crystals with different planes. *ACS Appl Mater Interfaces*. 2022;14(34):39591-39600.
11. Andreev SV, Aseev SA, Bagratashvili VN, et al. Ultrafast transmission electron microscope for studying the dynamics of the processes induced by femtosecond laser beams. *Quantum Electron*. 2017;47(2):116-122.
12. Zhu C, Zheng D, Wang H, et al. Development of analytical ultrafast transmission electron microscopy based on laser-driven Schottky field emission. *Ultramicroscopy*. 2020;209:112887.
13. Zhang M, Li Z-A, Sun S, et al. High spatiotemporal resolution of magnetic dynamics in Mn-Ni-Ga via four-dimensional Lorentz microscopy. *Phys Rev Appl*. 2019;12(3):034037.
14. Berruto G, Madan I, Murooka Y, et al. Laser-induced skyrmion writing and erasing in an ultrafast Cryo-Lorentz transmission electron microscope. *Phys Rev Lett*. 2018;120(11):117201.
15. Zhang M, Cao G, Tian H, et al. Picosecond view of a martensitic transition and nucleation in the shape memory alloy $Mn_{50}Ni_{40}Sn_{10}$ by four-dimensional transmission electron microscopy. *Phys Rev B*. 2017;96(17):174203.
16. Fu X, Liu S, Chen B, Tang J, Zhu Y. Observation and control of unidirectional ballistic dynamics of nanoparticles at a liquid-gas interface by 4D electron microscopy. *ACS Nano*. 2021;15(4):6801-6810.
17. Liao B, Zhao H, Najafi E, et al. Spatial-Temporal imaging of anisotropic photocarrier dynamics in black phosphorus. *Nano Lett*. 2017;17(6):3675-3680.
18. Wang F, Jiang L, Sun J, et al. One-step fabrication method of GaN films for internal quantum efficiency enhancement and their ultrafast mechanism investigation. *ACS Appl Mater Interfaces*. 2021;13(6):7688-7697.
19. Gong Y, Joly AG, Hu D, El-Khoury PZ, Hess WP. Ultrafast imaging of surface plasmons propagating on a gold surface. *Nano Lett*. 2015;15(5):3472-3478.
20. Voss JM, Harder OF, Olshin PK, Drabbels M, Lorenz UJ. Rapid melting and revitrification as an approach to microsecond time-resolved cryo-electron microscopy. *Chem Phys Lett*. 2021;778:138812.
21. Wu Q, Chen L, Wu Z, Lei L, Yao Y. Design and demonstration of a flexibly cascaded N-ring-cavity ultrafast soliton all-fiber laser based on circulators. *Opt Laser Technol*. 2022;152:108181.
22. Chang G, Wei Z. Ultrafast fiber lasers: an expanding versatile toolbox. *Iscience*. 2020;23(5):101101.
23. Fu W, Wright LG, Sidorenko P, Backus S, Wise FW. Several new directions for ultrafast fiber lasers. *Opt Express*. 2018;26(8):9432-9463.
24. Fermann ME, Hartl I. Ultrafast fiber laser technology. *IEEE J Sel Top Quantum Electron*. 2009;15(1):191-206.
25. Wu X, Peng J, Boscolo S, Zhang Y, Finot C, Zeng H. Intelligent breathing soliton generation in ultrafast fiber lasers. *Laser Photon Rev*. 2022;16(2):2100191.
26. Peng J, Zhao Z, Boscolo S, et al. Breather molecular complexes in a passively mode-locked fiber laser. *Laser Photon Rev*. 2021;15(7):2000132.
27. Tsai M-S, Liang A-Y, Tsai C-L, Lai P-W, Lin M-W, Chen M-C. Nonlinear compression toward high-energy single-cycle pulses by cascaded focus and compression. *Sci Adv*. 2022;8(31):eabo1945.
28. Su Y, Fang S, Gao Y, Zhao K, Chang G, Wei Z. Efficient generation of UV-enhanced intense supercontinuum in solids: toward sub-cycle transient. *Appl Phys Lett*. 2021;118(26):261102.
29. Gao Y, Su Y, Xu S, et al. Generation of annular femtosecond few-cycle pulses by self-compression and spatial filtering in solid thin plates. *Opt Express*. 2021;29(19):29789-29801.

30. Tang H, Men T, Liu X, et al. Single-shot compressed optical field topography. *Light Sci Appl*. 2022;11(1):244.
31. Yao Y, He Y, Qi D, et al. Single-shot real-time ultrafast imaging of femtosecond laser fabrication. *ACS Photon*. 2021;8(3):738-744.
32. Wang F, Jiang L, Pan C, et al. Hologram imaging quality improvement by ionization controlling based on the self-trapped excitons with double-pulse femtosecond laser. *Nanophotonics*. 2022;11(21):4727-4736.
33. Pan C, Jiang L, Sun J, et al. Ultrafast optical response and ablation mechanisms of molybdenum disulfide under intense femtosecond laser irradiation. *Light Sci Appl*. 2020;9(1):1-8.
34. Lian Y, Hua Y, Sun J, et al. Martensitic transformation in temporally shaped femtosecond laser shock peening 304 steel. *Appl Surf Sci*. 2021;567:150855.
35. Viotti A-L, Seidel M, Escoto E, et al. Multi-pass cells for post-compression of ultrashort laser pulses. *Optica*. 2022;9(2):197-216.
36. Pupeza I, Zhang C, Högner M, Ye J. Extreme-ultraviolet frequency combs for precision metrology and attosecond science. *Nat Photon*. 2021;15(3):175-186.
37. Kim JS, LaGrange T, Reed BW, et al. Imaging of transient structures using nanosecond in situ TEM. *Science*. 2008;321(5895):1472-1475.
38. Polli D, Brida D, Mukamel S, Lanzani G, Cerullo G. Effective temporal resolution in pump-probe spectroscopy with strongly chirped pulses. *Phys Rev A*. 2010;82(5):053809.
39. Grinblat G, Abdelwahab I, Nielsen MP, et al. Ultrafast all-optical modulation in 2D hybrid perovskites. *ACS Nano*. 2019;13(8):9504-9510.
40. Yang DS, Mohammed OF, Zewail AH. Scanning ultrafast electron microscopy. *Proc Natl Acad Sci USA*. 2010;107(34):14993-14998.
41. Zewail AH. Four-dimensional electron microscopy. *Science*. 2010;328(5975):187-193.
42. Flannigan DJ, Zewail AH. 4D electron microscopy: principles and applications. *Acc Chem Res*. 2012;45(10):1828-1839.
43. Zewail AH. Laser femtochemistry. *Science*. 1988;242(4886):1645-1653.
44. Zewail AH. Femtochemistry: atomic-scale dynamics of the chemical bond. *J Phys Chem A*. 2000;104(24):5660-5694.
45. Zewail AH. Femtochemistry: atomic-scale dynamics of the chemical bond using ultrafast lasers. *Angew Chem Int Ed*. 2000;39(15):2586-2631.
46. Klimov VI. Optical nonlinearities and ultrafast carrier dynamics in semiconductor nanocrystals. *J Phys Chem B*. 2000;104(26):6112-6123.
47. Dawlaty JM, Shivaraman S, Chandrashekhar M, Rana F, Spencer MG. Measurement of ultrafast carrier dynamics in epitaxial graphene. *Appl Phys Lett*. 2008;92(4):042116.
48. Rawalekar S, Kaniyankandy S, Verma S, Ghosh HN. Ultrafast charge carrier relaxation and charge transfer dynamics of CdTe/CdS core-shell quantum dots as studied by femtosecond transient absorption spectroscopy. *J Phys Chem C*. 2010;114(3):1460-1466.
49. Terada Y, Yoshida S, Takeuchi O, Shigekawa H. Real-space imaging of transient carrier dynamics by nanoscale pump-probe microscopy. *Nat Photonics*. 2010;4(12):869-874.
50. Lai T-H, Katsumata K, Hsu Y-J. In situ charge carrier dynamics of semiconductor nanostructures for advanced photoelectrochemical and photocatalytic applications. *Nanophotonics*. 2020;10(2):777-795.
51. Gélvez-Rueda MC, Renaud N, Grozema FC. Temperature dependent charge carrier dynamics in formamidinium lead iodide perovskite. *J Phys Chem C*. 2017;121(42):23392-23397.
52. Garming MWH, Bolhuis M, Conesa-Boj S, Kruit P, Hoogenboom JP. Lock-in ultrafast electron microscopy simultaneously visualizes carrier recombination and interface-mediated trapping. *J Phys Chem Lett*. 2020;11(20):8880-8886.
53. Shaheen BS, El-Zohry AM, Yin J, et al. Visualization of charge carrier trapping in silicon at the atomic surface level using four-dimensional electron imaging. *J Phys Chem Lett*. 2019;10(8):1960-1966.
54. Liu H, Wang C, Zuo Z, Liu D, Luo J. Direct visualization of exciton transport in defective few-layer WS(2) by ultrafast microscopy. *Adv Mater*. 2020;32(2):1906540.
55. Zhu T, Wan Y, Guo Z, Johnson J, Huang L. Two birds with one stone: tailoring singlet fission for both triplet yield and exciton diffusion length. *Adv Mater*. 2016;28(34):7539-7547.
56. Zhu T, Yuan L, Zhao Y, et al. Highly mobile charge-transfer excitons in two-dimensional WS2/tetracene heterostructures. *Sci Adv*. 2018;4(1):eaao3104.
57. Lian Y, Jiang L, Sun J, et al. Asymmetric response optoelectronic device based on femtosecond-laser-irradiated perovskite. *ACS Appl Mater Interfaces*. 2020;12(14):17070-17076.
58. Kusch G, Comish EJ, Loeto K, et al. Carrier dynamics at trench defects in InGaN/GaN quantum wells revealed by time-resolved cathodoluminescence. *Nanoscale*. 2022;14(2):402-409.
59. de Quilettes DW, Vorpahl SM, Stranks SD, et al. Impact of microstructure on local carrier lifetime in perovskite solar cells. *Science*. 2015;348(6235):683-686.
60. Yan L, Ma J, Li P, et al. Charge-carrier transport in quasi-2D Ruddlesden-Popper perovskite solar cells. *Adv Mater*. 2022;34(7):2106822.
61. Guo Z, Wan Y, Yang M, Snaider J, Zhu K, Huang L. Long-range hot-carrier transport in hybrid perovskites visualized by ultrafast microscopy. *Science*. 2017;356(6333):59-62.
62. Najafi E, Scarborough TD, Tang J, Zewail A. Four-dimensional imaging of carrier interface dynamics in pn junctions. *Science*. 2015;347(6218):164-167.
63. Wu S, Cheng OH-C, Zhao B, et al. The connection between plasmon decay dynamics and the surface enhanced Raman spectroscopy background: inelastic scattering from non-thermal and hot carriers. *J Appl Phys*. 2021;129(17):173103.
64. Ghahari F, Xie H-Y, Taniguchi T, Watanabe K, Foster MS, Kim P. Enhanced thermoelectric power in graphene: violation of the Mott relation by inelastic scattering. *Phys Rev Lett*. 2016;116(13):136802.
65. Dal Forno S, Lischner J. Electron-phonon coupling and hot electron thermalization in titanium nitride. *Phys Rev Mater*. 2019;3(11):115203.
66. Liang J, Wang LV. Single-shot ultrafast optical imaging. *Optica*. 2018;5(9):1113-1127.
67. Qi D, Zhang S, Yang C, et al. Single-shot compressed ultrafast photography: a review. *Adv Photon*. 2020;2(1):1.
68. Shin J, Gamage GA, Ding Z, et al. High ambipolar mobility in cubic boron arsenide. *Science*. 2022;377(6604):437-440.
69. Zhu T, Snaider JM, Yuan L, Huang L. Ultrafast dynamic microscopy of carrier and exciton transport. *Annu Rev Phys Chem*. 2019;70:219-244.
70. Gabriel MM, Kirschbrown JR, Christesen JD, et al. Direct imaging of free carrier and trap carrier motion in silicon nanowires by spatially-separated femtosecond pump-probe microscopy. *Nano Lett*. 2013;13(3):1336-1340.
71. Gabriel MM, Grumstrup EM, Kirschbrown JR, et al. Imaging charge separation and carrier recombination in nanowire pin junctions using ultrafast microscopy. *Nano Lett*. 2014;14(6):3079-3087.
72. Grumstrup EM, Gabriel MM, Cating EM, et al. Ultrafast carrier dynamics in individual silicon nanowires: characterization of diameter-dependent carrier lifetime and surface recombination with pump-probe microscopy. *J Phys Chem C*. 2014;118(16):8634-8640.
73. Guo Z, Manser JS, Wan Y, Kamat PV, Huang L. Spatial and temporal imaging of long-range charge transport in perovskite thin films by ultrafast microscopy. *Nat Commun*. 2015;6(1):7471.

74. Sun Q, Ueno K, Yu H, Kubo A, Matsuo Y, Misawa H. Direct imaging of the near field and dynamics of surface plasmon resonance on gold nanostructures using photoemission electron microscopy. *Light Sci Appl*. 2013;2(12):e118.
75. Verhoeven W, van Rens JFM, Kieft ER, Mutsaers PHA, Luiten OJ. High quality ultrafast transmission electron microscopy using resonant microwave cavities. *Ultramicroscopy*. 2018;188:85-89.
76. Houdellier F, Caruso GM, Weber S, Kociak M, Arbouet A. Development of a high brightness ultrafast transmission electron microscope based on a laser-driven cold field emission source. *Ultramicroscopy*. 2018;186:128-138.
77. Sun S, Sun X, Bartles D, et al. Direct imaging of plasma waves using ultrafast electron microscopy. *Struct Dyn*. 2020;7(6):064301.
78. Priebe KE, Rathje C, Yalunin SV, et al. Attosecond electron pulse trains and quantum state reconstruction in ultrafast transmission electron microscopy. *Nat Photonics*. 2017;11(12):793-797.
79. Bücker K, Picher M, Crégut O, et al. Ultrafast transmission electron microscopy reveals electron dynamics and trajectories in a thermionic gun setup. In: *European Microscopy Congress 2016: Proceedings*. Wiley; 2016:445-446.
80. Feist A, Bach N, Rubiano da Silva N, et al. Ultrafast transmission electron microscopy using a laser-driven field emitter: femtosecond resolution with a high coherence electron beam. *Ultramicroscopy*. 2017;176:63-73.
81. Bose R, Sun J, Khan JI, et al. Real-space visualization of energy loss and carrier diffusion in a semiconductor nanowire array using 4D electron microscopy. *Adv Mater*. 2016;28(25):5106-5111.
82. Shaheen BS, El-Zohry AM, Zhao J, et al. Real-space mapping of surface-oxygen defect states in photovoltaic materials using low-voltage scanning ultrafast electron microscopy. *ACS Appl Mater Interfaces*. 2020;12(6):7760-7767.
83. Feist A, Echternkamp KE, Schauss J, Yalunin SV, Schäfer S, Ropers C. Quantum coherent optical phase modulation in an ultrafast transmission electron microscope. *Nature*. 2015;521(7551):200-203.
84. Wong EL, Winchester AJ, Pareek V, Madéo J, Man MKL, Dani KM. Pulling apart photoexcited electrons by photoinducing an in-plane surface electric field. *Sci Adv*. 2018;4(9):eaat9722.
85. Spektor G, Prinz E, Hartelt M, Mahro A-K, Aeschlimann M, Orenstein M. Orbital angular momentum multiplication in plasmonic vortex cavities. *Sci Adv*. 2021;7(33):eabg5571.
86. Tromp RM, Hannon JB, Ellis AW, Wan W, Berghaus A, Schaff O. A new aberration-corrected, energy-filtered LEEM/PEEM instrument. I. Principles and design. *Ultramicroscopy*. 2010;110(7):852-861.
87. Zheng W, Jiang P, Zhang L, et al. Ultrafast extreme ultraviolet photoemission electron microscope. *Rev Sci Instrum*. 2021;92(4):043709.
88. Seiler H. Secondary electron emission in the scanning electron microscope. *J Appl Phys*. 1983;54(11):R1-R18.
89. Goldstein JI, Newbury DE, Michael JR, Ritchie NW, Scott JHJ, Joy DC. *Scanning Electron Microscopy and X-Ray Microanalysis*. Springer; 2017.
90. Vanacore GM, Fitzpatrick AWP, Zewail AH. Four-dimensional electron microscopy: ultrafast imaging, diffraction and spectroscopy in materials science and biology. *Nano Today*. 2016;11(2):228-249.
91. Barwick B, Zewail AH. Photonics and plasmonics in 4D ultrafast electron microscopy. *ACS Photonics*. 2015;2(10):1391-1402.
92. Kohl H, Reimer L. *Transmission Electron Microscopy*. Springer Series in Optical Sciences. Vol 36. Springer; 2008.
93. Park HS, Baskin JS, Barwick B, Kwon OH, Zewail AH. 4D ultrafast electron microscopy: imaging of atomic motions, acoustic resonances, and Moiré fringe dynamics. *Ultramicroscopy*. 2009;110(1):7-19.
94. Plemmons DA, Tae Park S, Zewail AH, Flannigan DJ. Characterization of fast photoelectron packets in weak and strong laser fields in ultrafast electron microscopy. *Ultramicroscopy*. 2014;146:97-102.
95. Man MKL, Margiolakis A, Deckoff-Jones S, et al. Imaging the motion of electrons across semiconductor heterojunctions. *Nat Nanotechnol*. 2017;12(1):36-40.
96. Chen R, Ren Z, Liang Y, et al. Spatiotemporal imaging of charge transfer in photocatalyst particles. *Nature*. 2022;610(7931):296-301.
97. Xue Z, Liao X, Li Y, et al. Photoexcited electron dynamics in $Cd_3As_2$ revealed by time- and energy-resolved photoemission electron microscopy. *J Phys Chem C*. 2022;126(6):3134-3139.
98. Adhikari A, Eliason JK, Sun J, Bose R, Flannigan DJ, Mohammed OF. Four-dimensional ultrafast electron microscopy: insights into an emerging technique. *ACS Appl Mater Interfaces*. 2017;9(1):3-16.
99. Khan JI, Adhikari A, Sun J, et al. Enhanced optoelectronic performance of a passivated nanowire-based device: key information from real-space imaging using 4D electron microscopy. *Small*. 2016;12(17):2313-2320.
100. Pan J, Liu S, Tang J. Ultrafast dynamics of photoinduced terahertz electron-hole plasma waves in semiconductor junctions. *Phys Rev B*. 2021;104(4):045309.
101. El-Zohry AM, Shaheen BS, Burlakov VM, et al. Extraordinary carrier diffusion on CdTe surfaces uncovered by 4D electron microscopy. *Chem*. 2019;5(3):706-718.
102. Plemmons DA, Suri PK, Flannigan DJ. Probing structural and electronic dynamics with ultrafast electron microscopy. *Chem Mater*. 2015;27(9):3178-3192.
103. Danz T, Domröse T, Ropers C. Ultrafast nanoimaging of the order parameter in a structural phase transition. *Science*. 2021;371(6527):371-374.
104. Fu X, Chen B, Li C, et al. Direct visualization of photomorphic reaction dynamics of plasmonic nanoparticles in liquid by four-dimensional electron microscopy. *J Phys Chem Lett*. 2018;9(14):4045-4052.
105. Zhang Y, Flannigan DJ. Observation of anisotropic strain-wave dynamics and few-layer dephasing in $MoS_2$ with ultrafast electron microscopy. *Nano Lett*. 2019;19(11):8216-8224.
106. Mo MZ, Chen Z, Li RK, et al. Heterogeneous to homogeneous melting transition visualized with ultrafast electron diffraction. *Science*. 2018;360(6396):1451-1455.
107. Qin Y, Ji B, Song X, Lin J. Disclosing transverse spin angular momentum of surface plasmon polaritons through independent spatiotemporal imaging of its in-plane and out-of-plane electric field components. *Photonics Res*. 2020;8(6):1042-1048.
108. Weng Y. Tracking the holistic evolution of charge transfer in a single photocatalyst particle. *Sci Bull*. 2022;67(23):2384-2386.
109. Qin Y, Ji B, Song X, Lin J. Ultrafast spatiotemporal control of directional launching of surface plasmon polaritons in a plasmonic nano coupler. *Photonics Res*. 2021;9(4):514-520.
110. Liao B, Najafi E, Li H, Minnich AJ, Zewail AH. Photo-excited hot carrier dynamics in hydrogenated amorphous silicon imaged by 4D electron microscopy. *Nat Nanotechnol*. 2017;12(9):871-876.
111. Zhao J, Nughays R, Bakr OM, Mohammed OF. Access to ultrafast surface and interface carrier dynamics simultaneously in space and time. *J Phys Chem C*. 2021;125(27):14495-14516.
112. Lundstrom M. *Fundamentals of Carrier Transport*. IOP Publishing; 2002.
113. Van Roosbroeck W, Casey Jr HC. Transport in relaxation semiconductors. *Phys Rev B*. 1972;5(6):2154-2175.
114. Bose R, Adhikari A, Burlakov VM, et al. Imaging localized energy states in silicon-doped InGaN nanowires using 4D electron microscopy. *ACS Energy Lett*. 2018;3(2):476-481.
115. Cho J, Hwang TY, Zewail AH. Visualization of carrier dynamics in p (n)-type GaAs by scanning ultrafast electron microscopy. *Proc Natl Acad Sci USA*. 2014;111(6):2094-2099.

116. Zhang Y, Flannigan DJ. Imaging nanometer phonon softening at crystal surface steps with 4D ultrafast electron microscopy. *Nano Lett*. 2021;21(17):7332-7338.
117. Yun SJ, Choi SH, Kim J-W, et al. Internal thermal stress-driven phase transformation in Van der Waals layered materials. *ACS Nano*. 2022;16(10):17033-17040.
118. Chen P, Chan Y-H, Liu R-Y, et al. Dimensional crossover and symmetry transformation of charge density waves in VSe2. *Phys Rev B*. 2022;105(16):L161404.

## AUTHOR BIOGRAPHIES

**Yiling Lian** is currently a PhD candidate at the School of Mechanical Engineering, Beijing Institute of Technology. His main research interests include ultrafast carrier/plasma/shockwave dynamics observation, micro/nano scale heat and mass transfer, and laser-induced ablation mechanism.

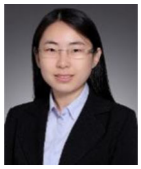

**Jingya Sun** is currently an associate professor at the School of Mechanical Engineering, Beijing Institute of Technology. She received her PhD degree from the National University of Singapore. Her research interests include four-dimensional in situ investigation of carrier dynamics in micro–nano optoelectronic materials and devices, as well as the multiscale observation and control of complex dynamics in femtosecond laser processing.

**Lan Jiang** is currently the chair professor of the Beijing Institute of Technology. He received his PhD degree in Mechanical Engineering from the Beijing Institute of Technology. He is the Changjiang professor (Ministry of Education, China), Russell Severance Springer Professor of UC Berkeley, OSA fellow, ASME fellow, and ISNM fellow. He has been a guest professor at the University of Nebraska-Lincoln and the Missouri University of Science and Technology. He has received many awards such as the Ho Leung Ho Lee Foundation Innovation Prize and the Second Prize of the National Natural Science Award (China). His research interests include modeling, method, measurement, and application in laser micro/nano fabrication.

**How to cite this article:** Lian Y, Sun J, Jiang L. Probing electron and lattice dynamics by ultrafast electron microscopy: principles and applications. *Int J Mech Syst Dyn*. 2023;3:192-212. doi:10.1002/msd2.12081